Brigham Young University
Department of Electrical and Computer Engineering

459 Clyde Building
Provo, Utah 84602

Optimization of SIRF for NSCAT

Quinn P. Remund
David G. Long, Ph.D.

3 July 1997

MERS Technical Report # MERS 97-03
ECEN Department Report # TR-L110-97.3

Microwave Earth Remote Sensing (MERS) Laboratory

Optimization of SIRF for NSCAT

Quinn P. Remund and David G. Long
Brigham Young University

July 2, 1997

Abstract

Scatterometers have historically been designed and used for ocean wind measurement. Scatterometer data has nominally low spatial resolution and until recently has had limited land/ice applications. However, resolution enhancement techniques can be used to broaden the applicability of scatterometer data. In particular, the SIRF algorithm, which uses several passes of the satellite to enhance the effective resolution, can increase the utility of scatterometer data. SIRF was originally developed for SASS which had different sampling characteristics. In this report SIRF is optimized for use with NSCAT data. Several parameters of the SIRF algorithm affect the estimation of the $\mathcal{A}$ and $\mathcal{B}$ values which describe the properties of σ^o. In this report SIRF initialization values are examined to determine optimum values. Accelerated $\mathcal{B}$ updates are used to decrease convergence time. Simulations of synthetic data are performed to monitor statistical error and correlation properties of the SIRF images. Incidence angle distribution factors are addressed. Optimum SIRF parameters for NSCAT data are presented.

1 Introduction

The NASA scatterometer (NSCAT) aboard the Japanese Advanced Earth Observation Satellite (ADEOS) was designed specifically to measure wind speeds and directions over the ocean surface. The rapid repeat coverage of scatterometers such as NSCAT makes them useful for the study of large scale phenomena. NSCAT is a dual polarization Ku-band instrument that exhibits higher intrinsic spatial resolution as well as more surface coverage than previous scatterometers [10]. While spaceborne scatterometers have been used to study non-ocean surface parameters (e.g. [1] [2] [3] [4] [5]), the low resolution is a limiting factor for land and ice studies. Resolution enhancement can make NSCAT data even more useful in non-ocean studies.

The Scatterometer Image Reconstruction with Filtering (SIRF) algorithm was developed [6] to enhance scatterometer data resolution by combining data from multiple passes of the satellite. This is done under the assumption that the observed surface region has minimal σ^o temporal variability during the observation period. This is generally the case for land and ice regions. From an initial estimate, SIRF iteratively updates estimates of σ^o until satisfactory convergence is reached. Since SIRF was originally developed for SASS data, the algorithm needs to be "tuned" for NSCAT.

Several SIRF algorithm parameters influence its effectiveness in resolution enhancement. Initialization values, update weighting, iteration number, and data incidence angle sampling all influence the functionality of the SIRF algorithm. This paper describes

the procedure taken to optimize SIRF for NSCAT data. Section 2 gives an overview of the SIRF algorithm. Section 3 covers the generation of simulated data for optimization tests. Section 4 discusses $\mathcal{B}$ value weighting and convergence in the algorithm. SIRF initialization is examined in section 5. In section 6, nonhomogeneous simulated SIRF images are created and statistical correlation and error analyses are performed. Incidence angle sampling is addressed in section 7. Finally, section 8 gives the conclusions drawn from this study.

2 SIRF Algorithm

The SIRF algorithm generates estimates for the $\mathcal{A}$ and $\mathcal{B}$ values for a given pixel from NSCAT σ^o and incidence angle (θ) measurements. Over a limited θ range of [20°-58°], σ^o is a approximately a linear function of θ,

$$10 \log_{10} \sigma^o(\theta) = \mathcal{A} + \mathcal{B}(\theta - 40^\circ) \tag{1}$$

where $\mathcal{A}$ and $\mathcal{B}$ are functions of surface characteristics, azimuth angle, and polarization. $\mathcal{A}$ is the σ^o value at 40° incidence and $\mathcal{B}$ describes the dependence of σ^o on θ. $\mathcal{A}$ and $\mathcal{B}$ provide valuable information about the surface. An angle of 40 degrees is chosen as a mid-swath value, though any interior swath angle can be used [9].

In this section, the method for obtaining enhanced resolution radar images of $\mathcal{A}$ and $\mathcal{B}$ in Eq. (1) from the low resolution scatterometer measurements is described. The method is based on the spatial overlap of the σ^o measurements from multiple scatterometer passes and on image reconstruction techniques. In order to develop the technique we first describe the enhanced resolution measurement model. We consider the effects of the scatterometer measurement noise and then describe methods for resolution enhancement of $\mathcal{A}$ and $\mathcal{B}$. A sample image output from SIRF is shown in Figure 1.

An understanding of NSCAT swath and cell geometry is needed to implement the SIRF algorithm using NSCAT data. NSCAT relies on six antennas (3 on each side of the satellite) to collect σ^o measurements. Each antenna is oriented at a different azimuth angle making a fan beam footprint on the surface. All antennas operate at vertical polarization and two of the antennas operate at both vertical and horizontal polarizations. Figure 2 illustrates the antenna illumination patterns on the surface. As the satellite travels forward, measurements are taken from two swaths, one on each side of the subsatellite track. Both the right and the left side swaths are 600 km wide with a gap of 350 km in between. The individual fan beam patterns are further resolved through Doppler filtering resulting in 25 individual cells within the footprint. Figure 3 shows the cell locations and geometries for 11 actual NSCAT measurements from each antenna. The monitor cells at 10° incidence were not plotted since they are not used in the imaging process. SIRF uses the overlap of these cells from multiple beams and multiple orbital passes of the satellite to enhance the resolution.

2.1 Enhanced Resolution σ^o Measurement Model

Consider a rectilinear grid of resolution elements on the earth's surface with a resolution element size of $S_x \times S_y$. The six-sided integrated resolution cells of the scatterometer measurements are imposed on this small-scale grid of resolution elements (refer to Fig.

4). Assuming a noise-free measurement, the value of σ^o measured by the scatterometer (denoted by ϱ_k where k is the measurement number) is a weighted average of the σ^o's of the individual resolution elements covered by the measurement cell, i.e.,

$$\varrho_k = \sum_{c=L_k}^{R_k} \sum_{a=B_k}^{T_k} h(x,y;k)\sigma^o(x,y;k) \tag{2}$$

where L_k, R_k, T_k, and B_k define a bounding rectangle for the k^{th} hexagonal σ^o measurement cell, $h(x,y;k)$ is the weighting function for the $(x,y)^{th}$ resolution element $(0 \leq h(x,y;k) \leq 1)$, and $\sigma^o(x,y;k)$ is the σ^o value for the $(x,y)^{th}$ resolution element. The incidence angle dependence of σ^o and h is subsumed in the k index. (Over a given scatterometer measurement cell the incidence angle θ is approximately constant.) h is a function of the cell location and shape.

The dependence of σ^o on θ can be expressed as [see Eq. (1)]

$$\sigma^o(\theta) = \alpha_o^{\mathcal{A}}[\beta_o(\theta)]^{\mathcal{B}} \tag{3}$$

with

$$\alpha_o = 10^{1/10} \tag{4}$$

$$\beta_o(\theta) = 10^{(40-\theta)/10}. \tag{5}$$

Using this relationship Eq. (2) can be written as

$$\varrho_k = \sum_{c=L_k}^{R_k} \sum_{a=B_k}^{T_k} h(x,y;k)\alpha_o^{\mathcal{A}(x,y)}[\beta_o(\theta_k)]^{\mathcal{B}(x,y)}. \tag{6}$$

The actual scatterometer measurements are noisy. Let z_k denote the noisy measurement of ϱ_k, then

$$z_k = \varrho_k + \nu_k \tag{7}$$

where ν_k is a zero-mean Gaussian random variable with variance

$$\mathrm{Var}[\nu_k] = \alpha\varrho_k^2 + \beta\varrho_k + \gamma \tag{8}$$

where α, β, and γ are from the K_p equation

$$K_p = \alpha\sigma^{o2} + \beta\sigma^o + \gamma \tag{9}$$

where α, β, and γ are known constants which depend on the measurement geometry (via the radar equation and the SNR) as well as the instrument parameters and calibration accuracy [10].

The resolution enhancement problem can then be posed as the following reconstruction problem: Given noisy measurements z_k of ϱ_k for $k \in [1,N]$, determine $\mathcal{A}(x,y)$ and $\mathcal{B}(x,y)$ for each element of the enhanced resolution grid. The method for solving this problem is described in the next section.

The key to successful resolution enhancement of $\mathcal{A}(x,y)$ and $\mathcal{B}(x,y)$ is taking advantage of the overlap in multiple measurements of the same general region. As will be discussed further, the ultimate $\mathcal{A}$ and $\mathcal{B}$ image resolutions are determined by this

measurement overlap. While measurements from the fore- and aft-facing antennas in a single orbit provide some measurement overlap, this overlap is generally insufficient to adequately apply the technique; hence, data from multiple orbits must be used.

In order to use data from multiple orbits we must assume the radar characteristics of the target region remain constant for each pass. Additionally, we assume that $\mathcal{A}$ and $\mathcal{B}$ have no azimuthal dependence. These and other requirements and assumptions needed (for SASS) are explored more fully in [8].

2.2 Reconstruction Approach

The Scatterometer Image Reconstruction algorithm (SIR) is based on multiplicative algebraic reconstruction (MART). Conventional single-variable MART is a special case of maximum entropy [7]. In MART, each measurement is compared to a predicted (forward projection) value computed from the current image estimate. A multiplicative correction factor is then applied each pixel covered by the measurement causing the forward projection to equal the measurement. Subsequent measurements further alter the pixel values. Over multiple iterations, the correction factors ideally converge to a value of unity and all the forward projections match the measurements. Unfortunately, MART has limited noise tolerance. SIR is a modified form of MART which has been optimized for noisy scatterometer measurements and to estimate both $\mathcal{A}$ and $\mathcal{B}$ in multivariate image reconstruction.

Initial estimates of $\mathcal{A}$ and $\mathcal{B}$, $\mathcal{A}_{init}$ and $\mathcal{B}_{init}$ images, are made by setting $\mathcal{B}_{init}$= the global average of $\mathcal{B}$ and $\mathcal{A}_{init}$= the global average of $\mathcal{A}$. In the k^{th} iteration of the SIR algorithm, the previous $\mathcal{B}$ estimate image is used to normalize the σ^o measurements from which an estimate of $\mathcal{A}$ is generated. Linear regression of the update terms (expressed at the measurement incidence angle) is then used to update the previous estimate of $\mathcal{B}$. The new $\mathcal{B}$ estimate is determined as a weighted average of the previous $\mathcal{B}$ estimate and the $\mathcal{B}$ estimate update. The multivariate SIR algorithm is given below [6].

We express the measurements z_j in dB so the forward projection f_j^k is computed in normal space while the $\mathcal{A}$ and $\mathcal{B}$ estimates are in log space, i.e.,

$$f_j^k = 10 \log_{10} \left[\frac{1}{q_j} \sum_{n=1}^{N} h_{jn} 10^{a_n^k/10} \right] \tag{10}$$

where q_j is defined in Eq. (12) and

$$p_i = \sum_{l=1}^{N} h_{li} \tag{11}$$

$$q_j = \sum_{l=1}^{M} h_{jl}. \tag{12}$$

Define d_{ij}^k as

$$d_{ij}^k = \left(\frac{z_j - b_i^k(\theta_j - 40^\circ)}{f_j^k} \right)^w. \tag{13}$$

The case with $w = 1$ will is unweighted MART while $w = 1/2$ is referred to as weighted MART and is used in SIRF. The $\mathcal{A}$ estimate update term, u_{ij}^k, is computed,

$$u_{ij}^k = \begin{cases} \left[\frac{1}{2}\frac{1}{f_j^k}\left(1 - \frac{1}{d_{ij}^k}\right) + \frac{1}{a_i^k d_{ij}^k}\right]^{-1} & d_{ij}^k \geq 1 \\ \left[\frac{1}{2} f_j^k \left(1 - d_{ij}^k\right) + a_i^k d_{ij}^k\right] & d_{ij}^k < 1 \end{cases} \tag{14}$$

with the $\mathcal{A}$ estimate, a_i^k, updated according to

$$a_i^{k+1} = \frac{1}{p_i} \sum_{j=1}^{N} h_{ji} u_{ij}^k. \tag{15}$$

To compute the $\mathcal{B}$ estimate, let

$$r_i = \sum_{j=1}^{N} h_{ji} \theta_j^2 \tag{16}$$

$$t_i = \sum_{j=1}^{N} h_{ji} \theta_j \tag{17}$$

and

$$\zeta_{ij}^k = u_{ij}^k + b_i^k (\theta_j - 40^\circ). \tag{18}$$

Then, the linear regression of the $\mathcal{A}$ updates, u_{ij}^k, provides an update for $\mathcal{B}$,

$$c_i^k = \frac{1}{p_i r_i - t_i^2} \left(p_i \sum_{j=1}^{N} h_{ji} \theta_j \zeta_{ij}^k - t_i \sum_{j=1}^{N} h_{ji} \zeta_{ij}^k \right). \tag{19}$$

This update is only usable if the range of incidence angles (θ_j) used in Eq. (19) is sufficiently wide. Since a wider incidence angle range implies greater confidence in the $\mathcal{B}$ estimate update [6], the $\mathcal{B}$ estimate is updated using a weighted average of c_i^k and the previous $\mathcal{B}$ estimate. The weighting factor is a simple function of the variance of θ, i.e., let

$$x_i = \frac{p_i}{t_i^2} \sum_{j=1}^{N} h_{ji} \theta_j^2 - 1 \tag{20}$$

then the $\mathcal{B}$ estimate image is updated according to

$$b_i^{k+1} = \frac{1}{x_i + 1} \left(x_i c_i^k + b_i^k \right). \tag{21}$$

This system of equations is iterated over k until convergence. Convergence is discussed in following sections.

The subjective quality of the final images can be improved by applying an edge-preserving 3×3 median filter to the $\mathcal{A}$ and $\mathcal{B}$ images. The image noise can be significantly reduced, with only a small reduction in the image resolution, by application of a hybrid median-linear filter to the image estimates at each stage of the iteration. The SIR algorithm with the added filtering is termed SIRF.

In the hybrid filter, the image values within a moving 3×3 window are ordered and the median determined. If the difference between the second highest and second lowest values within the window is less than 0.25, the center pixel is replaced with the average of the middle seven values of the ordered window pixels. Otherwise, the center value is replaced with the median value. Effectively, this hybrid filter acts like a linear filter when the algorithm is near convergence and the region is smooth but operates as a median filter otherwise. The edge-preserving properties of the median filter maintain resolution while providing noise suppression.

SIRF was originally developed for use with Seasat scatterometer (SASS) data [6]. The $\mathcal{B}$ updates were heavily damped in the original version of SIRF and may not be appropriate for NSCAT data. For NSCAT $\mathcal{B}$ value convergence can be accelerated by weighting these updates appropriately.

Equation (21) defines the iterative update for $\mathcal{B}$ based on a linear regression of the $\mathcal{A}$ updates c_i^k (Eq. (19)) and a weighting factor x_i determined by the variance of incidence angles (Eq. (20)). To facilitate convergence of the $\mathcal{B}$ values, the updates are further weighted with an acceleration factor b_{acc}. Using this approach, Eq. (20) becomes

$$x_i = b_{acc} \left(\frac{p_i}{t_i^2} \sum_{j=1}^{N} h_{ji} \theta_j^2 - 1 \right) \tag{22}$$

where b_{acc} is the acceleration factor ($b_{acc} > 1$). The selection of b_{acc} is described in a later section.

2.3 AVE Algorithm

As described in [6], a very simple approach to simultaneous estimation of $\mathcal{A}$ and $\mathcal{B}$ may be derived from the unweighted MART algorithm. For a constant initial value, the first iteration of unweighted MART is

$$a_i^1 = \frac{1}{p_i} \sum_{j=1}^{N} h_{ji} z_j. \tag{23}$$

Remembering that h_{ij} is either one or zero, we see that a_i^1 is the average of the measurements covering the i^{th} pixel. This averaging approach (which will be referred to as AVE) provides a smoothed initial image estimate which, in effect, is improved by later iterations of SIRF [6]. In AVE the $\mathcal{A}$ and $\mathcal{B}$ estimates for a given pixel are computed by linear regression of the σ^o measurements (in dB) which cover the pixel. We note that the AVE resolution is better than the measurement cell resolution and is significantly better than conventional "binning" where the minimum resolution element size is effectively limited to the maximum size of the measurement cells, but AVE resolution is not as good as SIR or SIRF.

3 Generating Simulation Data

The values of b_{acc}, the number of iterations of SIRF, $\mathcal{A}_{init}$, and $\mathcal{B}_{init}$ affect the estimated image accuracy and quality. In this section, simulations are used to select optimum parameter values. To examine the effects of these parameters, synthetic $\mathcal{A}$ and $\mathcal{B}$ truth

images are created. The images are created at higher resolution (approximately 4.5 km per pixel) than the nominal resolution of the satellite (25 km) with dimensions of approximately 8°×8°. Constant value images are used for both parameters. Two simulations are performed. The first has truth values $\mathcal{A}$=-10.0 $\mathcal{B}$=-0.1 and the second uses $\mathcal{A}$=-20.0 $\mathcal{B}$=-0.2.

NSCAT L1.5 data records contain geolocation, azimuth angle, incidence angle, σ^o, and noise information for each measurement cell. Simulated data is generated using 10 days of actual NSCAT data (1996 JD 301-310) taken from the Amazon Basin (latitude range of 2.0°S to 10.0°S, longitude range of 62.0°W to 70.0°W) combined with the truth images. The actual data provides geolocation and incidence angle information and the truth images are used to create synthetic σ^o and variance values. σ^o is computed from effective $\mathcal{A}$ and $\mathcal{B}$ values in the measurement footprint (see Figure 4),

$$A_{eff} = \sum_{c=L_k}^{R_k} \sum_{a=B_k}^{T_k} h(x,y;k) A_{truth}(x,y;k) \tag{24}$$

$$B_{eff} = \sum_{c=L_k}^{R_k} \sum_{a=B_k}^{T_k} h(x,y;k) B_{truth}(x,y;k) \tag{25}$$

where L_k, R_k, T_k, and B_k define a bounding rectangle for the k^{th} hexagonal σ^o measurement cell, $h(x,y;k)$ is the weighting function for the $(x,y)^{th}$ resolution element ($h(x,y;k)$=0 or 1 for NSCAT), $A_{truth}(x,y;k)$ is the $\mathcal{A}$ value for the $(x,y)^{th}$ resolution element, and $B_{truth}(x,y;k)$ is the corresponding $\mathcal{B}$ value. The noiseless σ^o then becomes

$$\sigma^o_{nl} = A_{eff} + B_{eff}(\theta - 40°). \tag{26}$$

Realistic noise is added to σ^o_{nl} by using actual variance values of the data. The variance of σ^o is a function of σ^o , α, β, and γ. The simulated σ^o is given by

$$\sigma^o = \sigma^o_{nl}(1 + K_p \nu) \tag{27}$$

where

$$K_p = \alpha \sigma^{o2}_{nl} + \beta \sigma^o_{nl} + \gamma \tag{28}$$

and ν is a zero-mean Gaussian random variable with unity variance. This is performed for all of the measurements cells in the study region during the time period 1996 JD 301-310.

4 $\mathcal{B}$ Weighting

The effects of $\mathcal{B}$ acceleration are studied by using the synthetic images described above. The truth image is $\mathcal{A}$=-10.0 and $\mathcal{B}$=-0.1. SIRF is implemented repeatedly with different $\mathcal{B}$ weighting values b_{acc}. Initialization values of $\mathcal{A}$=-10.0, -30.0 and $\mathcal{B}$=-0.1, -0.3 are used to evaluate worst case convergence scenarios.

The first case considered is $\mathcal{A}_{init}$=-30.0 and $\mathcal{B}_{init}$=-0.1 (the true $\mathcal{B}$ value). Figures 5-6 display the means and standard deviations of the $\mathcal{A}$ and $\mathcal{B}$ values for the SIRF images at each iteration and $\mathcal{B}$ weighting. The $\mathcal{A}$ mean converges to its actual value nearly identically regardless of the $\mathcal{B}$ weighting (b_{acc}), achieving its true value after

approximately 25 iterations. Increasing the $\mathcal{B}$ weighting slightly increases the $\mathcal{A}$ noise level as indicated by the $\mathcal{A}$ standard deviation. The mean for the $\mathcal{B}$ images diverges slightly from the true value for all $\mathcal{B}$ weights although the worst error after even 75 iterations is small (on the order of .0002 dB/deg). The $\mathcal{B}$ noise level also increases with $\mathcal{B}$ weighting although the noise is small.

Another simulation is run with $\mathcal{A}_{init}$=-10.0 (the true $\mathcal{A}$ value) and $\mathcal{B}_{init}$=-0.3 to observe the effects of $\mathcal{B}$ convergence alone. Figures 7-8 plot the results. The mean $\mathcal{A}$ value first diverges from its true value for the first several iterations. It then recovers and begins to converge back to the desired value at a rate determined by the $\mathcal{B}$ acceleration value. Higher $\mathcal{B}$ weights result in quicker convergence. The $\mathcal{A}$ standard deviation in the images initially increases for the first 5-15 iterations, then decreases converging to the same final value as in the $\mathcal{A}_{init}$=-30.0 $\mathcal{B}_{init}$=-0.1 case. Convergence is achieved more quickly for higher $\mathcal{B}$ acceleration values. From Figure 8 we see that $\mathcal{B}$ weighting is required to achieve convergence in less than 75 iterations. Increased $\mathcal{B}$ weighting speeds the convergence.

These simulations indicate that increasing the $\mathcal{B}$ weighting yields quicker convergence though excessive acceleration can increase the noise level of the image. If 50 iterations are used, a $\mathcal{B}$ update weight of 30 is sufficient to reach convergence in mean and standard deviation.

5 SIRF Initialization

SIRF requires initial values of $\mathcal{A}$ and $\mathcal{B}$. The algorithm iteratively updates the estimate by comparing the previous estimate with raw data values. The algorithm continues for N iterations. If a poor initialization value is used, the $\mathcal{A}$ and $\mathcal{B}$ values may not converge sufficiently accurately to the desired value within a given number of iterations.

To study the effects of different initialization values, simulated measurements are used to produce enhanced resolution SIRF images. SIRF is implemented several times for each image using different initialization values. For $\mathcal{A}_{init}$, values from -30.0 to -1.0 are used while $\mathcal{B}_{init}$ is set to various values in the range -0.3 to 0.0. $\mathcal{B}$ update weighting is set to b_{acc}=30 to ensure proper convergence of the $\mathcal{B}$ values. The mean and standard deviation of the resulting images are observed after each iteration.

The first case observed uses truth images with $\mathcal{A}$=-10.0 and $\mathcal{B}$=-0.1. Figures 9-10 illustrate the convergence trends of the means and standard deviations of the $\mathcal{A}$ and $\mathcal{B}$ images with iteration using different $\mathcal{A}_{init}$ values. The mean $\mathcal{A}$ converges to the true value for all $\mathcal{A}_{init}$'s by the 30th iteration. In general, the further $\mathcal{A}_{init}$ is from the true value, the longer it takes to converge. However, when $\mathcal{A}_{init}$ is less than the true value, the updates approach the desired value more quickly than if $\mathcal{A}_{init}$ is greater. The noise level in the image behaves similarly for all $\mathcal{A}_{init}$ values increasing with iteration number. Mean $\mathcal{B}$ diverges slightly from the true value. The $\mathcal{B}$ image noise grows with iteration until convergence.

Figures 11-12 show the results of various $\mathcal{B}_{init}$ for the same truth images. $\mathcal{A}_{init}$ is set to the true value while $\mathcal{B}_{init}$ ranges from -0.3 to 0.0. The mean $\mathcal{A}$ value of the SIRF image initially diverges from the true value but returns to the true value by the 50th iteration. The noise in the $\mathcal{A}$ image is significantly higher during the initial iterations when $\mathcal{B}_{init}$ is further away from the true $\mathcal{B}$. However, the noise levels converge for

later iterations. Similarly, the mean $\mathcal{B}$ converges to the actual value by about the 50th iteration. The $\mathcal{B}$ noise level converges to a common value for all $\mathcal{B}_{init}$ values.

The same experiment is conducted for the case with true values of $\mathcal{A}$=-20.0 and $\mathcal{B}$=-0.2. The results are shown in Figures 13-16. Behavior is the same observed in previous cases.

Several conclusions are drawn from this portion of the project. First, it is desirable for the initialization values to be close to the true values since they will converge more quickly. By setting $\mathcal{A}_{init}$ or $\mathcal{B}_{init}$ lower than the true value, convergence can be achieved earlier in the process. However, this effect is small and insignificant. Noise level is initially higher for these lower initialization values, but converges to a common value for all initializations for later iterations. These simulations were performed for constant $\mathcal{A}$ and $\mathcal{B}$ images. In a more realistic case the truth images will be nonhomogeneous with a wide range of $\mathcal{A}$ and $\mathcal{B}$ values. In an effort to balance the trade-off between convergence time and noise level, it was decided to use the means of the observed $\mathcal{A}$ and $\mathcal{B}$ images as the initial values.

To determine the optimum $\mathcal{A}_{init}$ and $\mathcal{B}_{init}$ for NSCAT SIRF images, accelerated $\mathcal{B}$ SIRF images are created for all land regions of the earth using NSCAT data during the period 1996 JD 276-281 to determine average $\mathcal{A}$ and $\mathcal{B}$ values. The averages are approximately $\mathcal{A}$=-8.4 $\mathcal{B}$=-0.14 (excluding polar regions). These values are chosen to be the $\mathcal{A}_{init}$ and $\mathcal{B}_{init}$ constant initialization images for SIRF.

6 Statistical Analysis of Simulated Images

With SIRF initialization values, number of iterations, and b_{acc} selected, the next step is to simulate SIRF using nonhomogeneous images and observe the statistical error and correlation properties between the SIRF images and the true images. Synthetic $\mathcal{A}$ and $\mathcal{B}$ truth images are created to emulate features that might be observed in actual scatterometer observations of the earth. The $\mathcal{A}$ truth image is shown in Figure 17 (a) while the corresponding $\mathcal{B}$ truth image is given in Figure 18 (a). The features of these images simulate features in actual NSCAT data. The darker area simulates a river body of water with characteristically low $\mathcal{A}$ or $\mathcal{B}$ values. The large feature in the top right quadrant of the $\mathcal{A}$ image represents an area with gradually increasing σ^o to a common center point. The two dots represent small features that SIRF will attempt to resolve. The rest of the image is assigned an average background value. The $\mathcal{B}$ image features are mirrored with respect to the $\mathcal{A}$ image to observe the effects of SIRF on $\mathcal{A}$ and $\mathcal{B}$ individually. The images are 192x192 pixels with and span of $8^\circ \times 8^\circ$ with a resolution of approximately 4.5 km/pixel.

6.1 SIRF Statistics

NSCAT data is simulated by using 10 days of real NSCAT data records over the Amazon Basin and replacing the σ^o values with synthetic σ^o values computed from the $\mathcal{A}$ and $\mathcal{B}$ truth image according to Eq. (1). Noisy data sets are generated. SIRF is run using the $\mathcal{A}$ and $\mathcal{B}$ initialization values determined previously ($\mathcal{A}_{init}$=-8.4, $\mathcal{B}_{init}$=-0.14). Several $\mathcal{B}$ weighting values are used and images are created after each iteration. Every image is then statistically compared with the truth image to determine error and correlation

properties. Metrics used in this development are mean error, standard deviation of the error, RMS error, and correlation coefficient.

Figures 19-22 depict the statistical error and correlation values for the SIRF $\mathcal{A}$ and $\mathcal{B}$ images as a function of iteration number and $\mathcal{B}$ update weighting. In all scenarios, all of the statistical metrics converge toward a final value as the algorithm iterates. The errors decrease and the correlation rises reaching their final values by the 50th iteration. The statistics for the $\mathcal{A}$ image behave similarly as iterations increase despite the different accelerated $\mathcal{B}$ values. On the other hand, the $\mathcal{B}$ image statistics are dependent on $\mathcal{B}$ update weighting. The mean error, error standard deviation, RMS error, and correlation coefficient reach their final optimum values more quickly for higher $\mathcal{B}$ acceleration. After 50 iterations, the statistics are virtually the same if the $\mathcal{B}$ weighting is 30 or higher.

The correlation coefficient for the $\mathcal{A}$ images approaches 0.95 while values of only about 0.40 are reached for the $\mathcal{B}$ images indicating that SIRF has excellent ability to estimate $\mathcal{A}$ but less accurate in determining $\mathcal{B}$. $\mathcal{B}$ estimate error may be the result of excessive σ^o noise or an insufficient distribution of incidence angles of the samples to accurately determine the σ^o incidence angle dependence. This problem is addressed in the next section.

6.2 Comparison of SIRF with Other Reconstruction Methods

$\mathcal{A}$ and $\mathcal{B}$ images of the simulation region are created using other reconstruction methods as well. Nonenhanced images are produced by gridding the NSCAT footprint σ^o values onto a 25 km grid and doing linear regression. AVE images [6] are created on the same high resolution grid that SIRF uses and is essentially equivalent to the first iteration of SIRF [6].

Figure 17 illustrates the $\mathcal{A}$ value truth, nonenhanced, AVE, and SIRF images. The SIRF image uses b_{acc}=30, N=50 iterations, $\mathcal{A}_{init}$=-8.4, and $\mathcal{B}_{init}$=-0.14. The nonenhanced image shows the general features, but does not define the smaller features well. The AVE image reveals more high frequency information but the edges still appear low-pass filtered. The SIRF image has sharper edges and more defined features. Still the source of the distortion in the average and SIRF images is due to the filtering of the surface truth data by the aperture of the scatterometer antenna as well as by the inherent scatterometer noise. Note that the dots stand out above the noise in the average and SIRF images.

The reconstructed $\mathcal{B}$ images are shown in Figure 18. An interesting ghost image phenomenon appears in all of the reconstructed images. That is, the $\mathcal{A}$ truth image features appear in the reconstructed $\mathcal{B}$ images and vice versa. This occurrence is most pronounced in the nonenhanced and AVE images with little effect in the SIRF image. Since the AVE image is essentially the output of the SIRF algorithm after one iteration, it is apparent that repeated iterations damp the distortion effects of $\mathcal{A}$ value on $\mathcal{B}$. The $\mathcal{B}$ images have lower correlation to the truth image since the slope of σ^o vs. θ is very sensitive to σ^o noise.

Statistical error and correlation metrics for each of these images are computed and given in Table 1. SIRF has lower errors and higher correlation coefficients for virtually all of the metrics. In every case, SIRF has a higher correlation coefficient and lower RMS error indicating that it was most successful in reconstructing the $\mathcal{A}$ and $\mathcal{B}$ images.

7 Sampling

The accuracy of SIRF $\mathcal{A}$ and $\mathcal{B}$ estimates is highly dependent on the number of σ^o samples for a given pixel. $\mathcal{B}$ contains incidence angle dependence information and cannot be properly estimated unless several measurements are obtained from a variety of incidence angles. Thus, incidence angle distribution as well as the number of measurements affect the effectiveness of the SIRF algorithm.

The incidence angle dependence of σ^o is described by the $\mathcal{B}$ parameter. SIRF uses several σ^o measurements of a pixel to estimate this value. To get a good estimate of $\mathcal{B}$ SIRF requires a sufficient number of different incidence angle (θ) measurements as well as a good distribution of θ. An experiment is conducted in which SIRF is run for a a simulation region with constant $\mathcal{A}$ and $\mathcal{B}$ values. Simulated σ^o measurements are generated from the true values. $\mathcal{A}$=-10.0 and $\mathcal{B}$=-0.1 are used as the actual values. The θ values for measurements over a small 3×3 pixel subregion are set to have a uniform distribution in the range [20°-58°]. SIRF $\mathcal{A}$ and $\mathcal{B}$ estimates are computed for various numbers of measurements. Figure 23 displays example $\mathcal{A}$ and $\mathcal{B}$ mean values in the subregion that SIRF predicts as a function of number of measurements. The plot demonstrates that for a low number of measurements, the SIRF estimates are inaccurate. When SIRF has about 5 σ^o samples or more, the estimates are close to the true value with error a function of the noise in the measurements.

The incidence angle distribution of the measurements affect the accuracy of SIRF estimates. The dependence of estimate error on this is examined by implementing a similar simulation as described above but the incidence angles are modified to various distributions. Different distributions of incidence angles are used and the estimates observed. The true values are $\mathcal{A}$=-10.0 and $\mathcal{B}$=-0.1. For each simulation, 8 measurements are used. SIRF computes $\mathcal{A}$ and $\mathcal{B}$ estimates for several measurement sets with different θ distributions. For each θ distribution set, SIRF is run 5 times (individual cases differing only in random σ^o noise) to exhibit the general trends. Figure 24 shows a plot of $\mathcal{A}$ estimates vs. $\mathcal{B}$ estimates for different distributions. Nearly every SIRF $\mathcal{A}$ estimate is within 0.1 dB of the actual value regardless of the θ distribution. Similarly, all of the $\mathcal{B}$ estimates have an error of less than 0.01 dB/deg. We conclude that SIRF yields good estimates of $\mathcal{A}$ and $\mathcal{B}$ for NSCAT even if the θ distribution is relatively narrow, at least for a surface where the linear σ^o model applies.

8 Conclusion

The Scatterometer Image Reconstruction with Filter (SIRF) algorithm is an effective method for high resolution image reconstruction. Several parameters of this algorithm affect its ability to enhance intrinsically low resolution scatterometer data to make it useful for non-oceanic studies. Through a non-linear procedure, SIRF iteratively updates $\mathcal{A}$ and $\mathcal{B}$ estimates to describe σ^o normalized to 40° and σ^o dependence on incidence angle.

Heavy damping of the $\mathcal{B}$ updates in the algorithm slow the convergence of $\mathcal{B}$ to the true value. $\mathcal{B}$ update weighting is used to speed this process. Simulations show that accelerating these updates reduces convergence time. Both $\mathcal{A}$ and $\mathcal{B}$ noise levels diverge for several iterations and then decrease, converging to a final value. This convergence occurs more quickly for higher $\mathcal{B}$ update weighting. After approximately 50 iterations,

there is little difference in the error and noise properties of the reconstructed image as long as the $\mathcal{B}$ acceleration is greater than or equal to 30.

SIRF initialization values strongly influence the convergence trends of the algorithm. When the initial values are close to the true values, convergence occurs more rapidly. When $\mathcal{A}_{init}$ and $\mathcal{B}_{init}$ are set below the true values rather than above, convergence was achieved slightly earlier in the iterations but noise level was increased. However, if enough iterations were used, convergence is to a common value for all initializations. This trade-off motivated the choice of the mean $\mathcal{A}$ and $\mathcal{B}$ values of nonhomogeneous regions for the initialization. $\mathcal{A}_{init}$=-8.4 and $\mathcal{B}_{init}$=-0.14 were found to be the mean global values for NSCAT land data (excluding polar regions) and thus chosen as the optimum initialization values.

Nonhomogeneous synthetic images are used to study the error and correlation properties between SIRF images and their ground truth counterparts. The statistical metrics continuously improve with increased iterations until a final value is reached after about 50 iterations.

In addition to these parameters, the measurement geometry can influence SIRF's effectiveness in estimating $\mathcal{A}$ and $\mathcal{B}$. In particular, the incidence angle distribution is critical to achieving good $\mathcal{B}$ values. Assuming a uniform distribution of θ in the effective range of [20°-58°], SIRF requires about 5 or more samples to produce quality $\mathcal{A}$ and $\mathcal{B}$ estimates. SIRF produces good estimates for relatively narrow θ distributions as well as wide distributions.

References

[1] D. G. Long and P. J. Hardin, "Vegetation Studies of the Amazon Basin Using Enhanced Resolution Seasat Scatterometer Data", *IEEE Transactions on Geoscience and Remote Sensing*, vol. 32, pp. 449–460, 1994.

[2] D. Long and M. Drinkwater, "Greenland Ice-Sheet Surface Properties Observed by the Seasat-A Scatterometer at Enhanced Resolution", *Journal of Glaciology*, vol. 40, no. 135, pp. 213–230, 1994.

[3] M. Drinkwater, D. Long, and D. Early, "Enhanced Resolution ERS-1 Scatterometer Imaging of Southern Ocean Sea Ice", *ESA Journal*, vol. 17, pp. 307–322, 1993.

[4] A. R. Hosseinmostafa, V. I. Lytle, K. C. Jezek, S. P. Gogineni, S. F. Ackley, and R. K. Moore, "Comparison of Radar Backscatter from Antarctic and Arctic Sea Ice", *Journal of Electromagnetic Waves and Applications*, vol. 9, no. 3, pp. 421–438, 1995.

[5] P. Lecomte, A. Cavanie, and F. Gohin, "Recognition of Sea Ice Zones using ERS-1 Scatterometer Data", in *Proceedings of IGARSS 93*. IEEE, 1993, pp. 855–857.

[6] D. Long, P. Hardin, and P. Whiting, "Resolution Enhancement of Spaceborne Scatterometer Data", *IEEE Transactions on Geoscience and Remote Sensing*, vol. 31, pp. 700–715, 1993.

[7] Y. Censor, "Finite Series-Expansion Reconstruction Methods," *Proceedings of the IEEE*, Vol. 71, No. 3, pp. 409-419, Mar. 1983.

[8] D. G. Long and P. J. Hardin,"Vegetation Studies of the Amazon Basin Using Enhanced Resolution Seasat Scatterometer Data," *IEEE Transactions on Geoscience and Remote Sensing*, Vol. 32, No. 2, March 1994.

[9] D. G. Long and D. S. Early, "Azimuthal Modulation of C-Band Scatterometer σ^o Over Southern Ocean Sea Ice," *to appear IEEE Transactions on Geoscience and Remote Sensing*, Sept. 1997.

[10] F. M. Naderi, M. H. Frielich, D. G. Long, "Spaceborne Radar Measurement of Wind Velocity Over the Ocean - An Overview of the NSCAT Scatterometer System," *Proceedings of the IEEE*, Vol. 79, No. 6, June 1991.

Tables

Image	Mean Error	Error Std.	RMS Error	Corr. Coeff.
Nonenhanced $\mathcal{A}$	-0.09	1.09	1.10	0.86
AVE $\mathcal{A}$	-0.10	1.07	1.07	0.86
SIRF $\mathcal{A}$	-0.05	0.68	0.68	0.95
Nonenhanced $\mathcal{B}$	-0.00004	0.093	0.093	0.233
AVE $\mathcal{B}$	0.004	0.140	0.140	0.187
SIRF $\mathcal{B}$	0.0004	0.057	0.057	0.40

Table 1: Error and correlation statistics of reconstructed noisy images as compared to the true images. SIRF was implemented using $\mathcal{A}_{init}$=-8.4, $\mathcal{B}_{init}$=-0.14, b_{acc}=30, and 50 iterations.

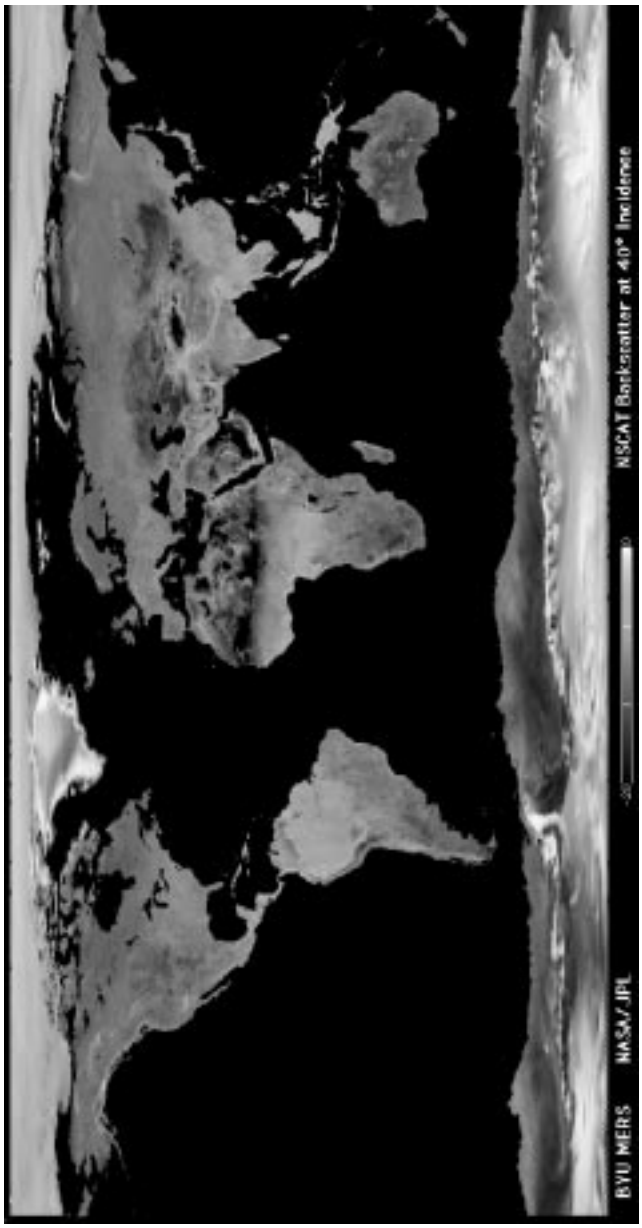

Figure 1: A global image made by SIRF. The image shows $\mathcal{A}$, the incidence angle normalized σ^o . The ocean has been masked out.

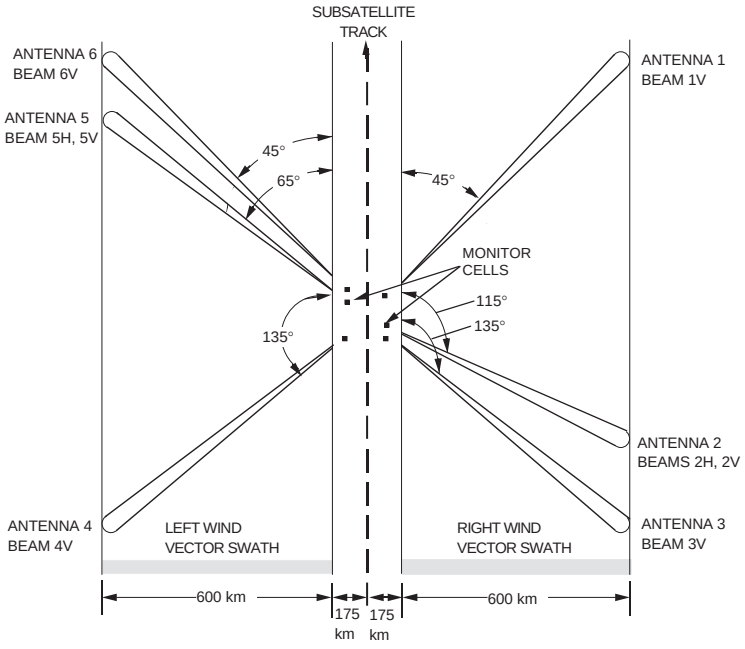

Figure 2: NSCAT antenna illumination patterns on the surface of the earth.

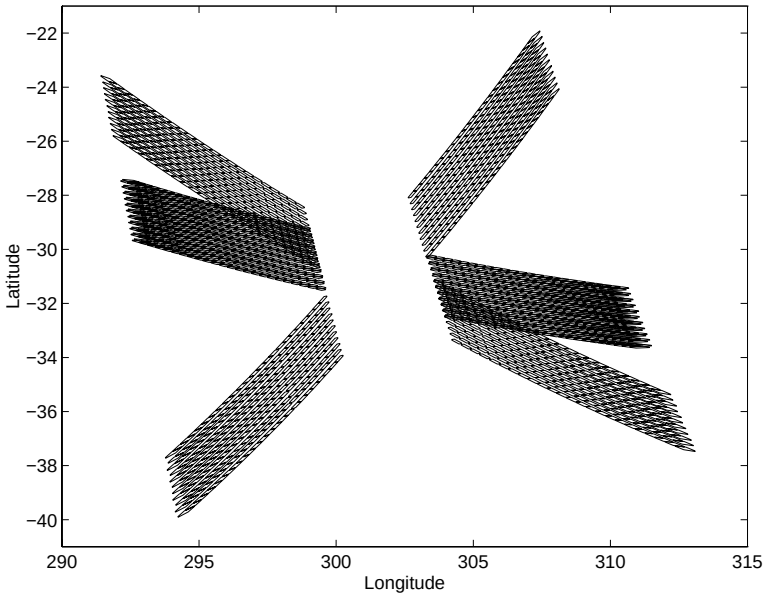

Figure 3: Actual NSCAT cell locations and geometries for 11 antenna cycles.

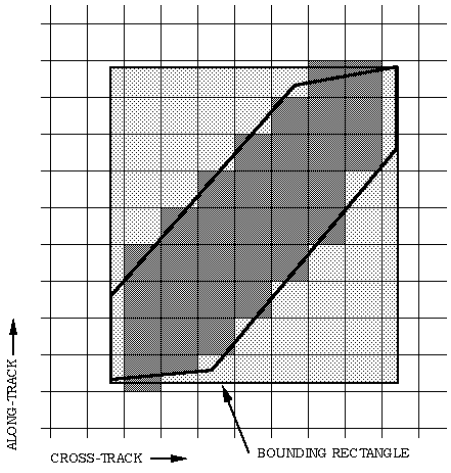

Figure 4: An integrated NSCAT σ^o cell overlaying the high resolution grid. Only the shaded square grid elements have nonzero $h(x, y; k)$. The bounding rectangle is also indicated.

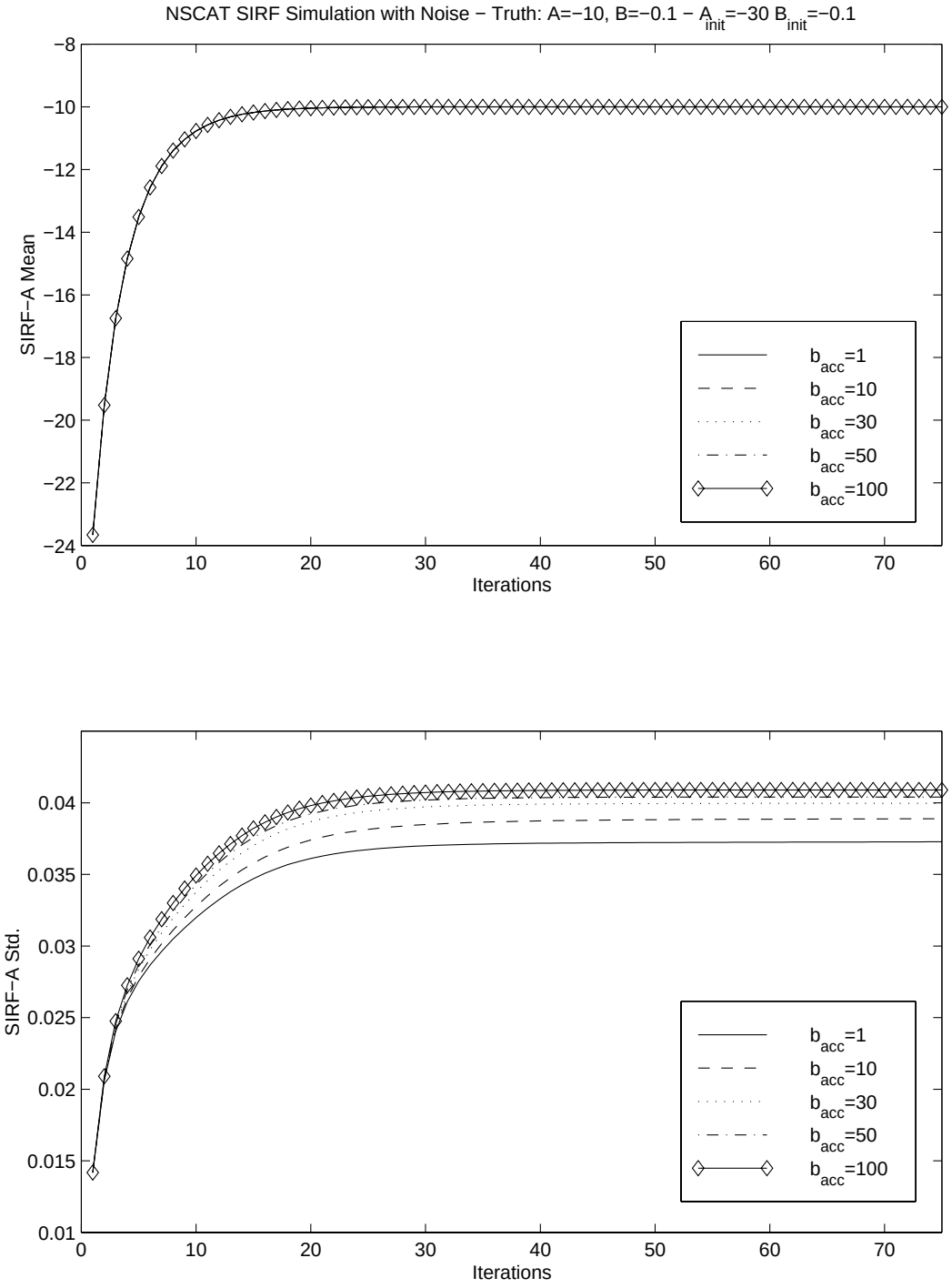

Figure 5: $\mathcal{A}$ value means and standard deviations of the SIRF simulation images with constant truth images $\mathcal{A}$=-10.0 and $\mathcal{B}$=-0.1. Initialization values are $\mathcal{A}_{init}$=-30.0 and $\mathcal{B}_{init}$=-0.1. Different values of $\mathcal{B}$ update weight are used.

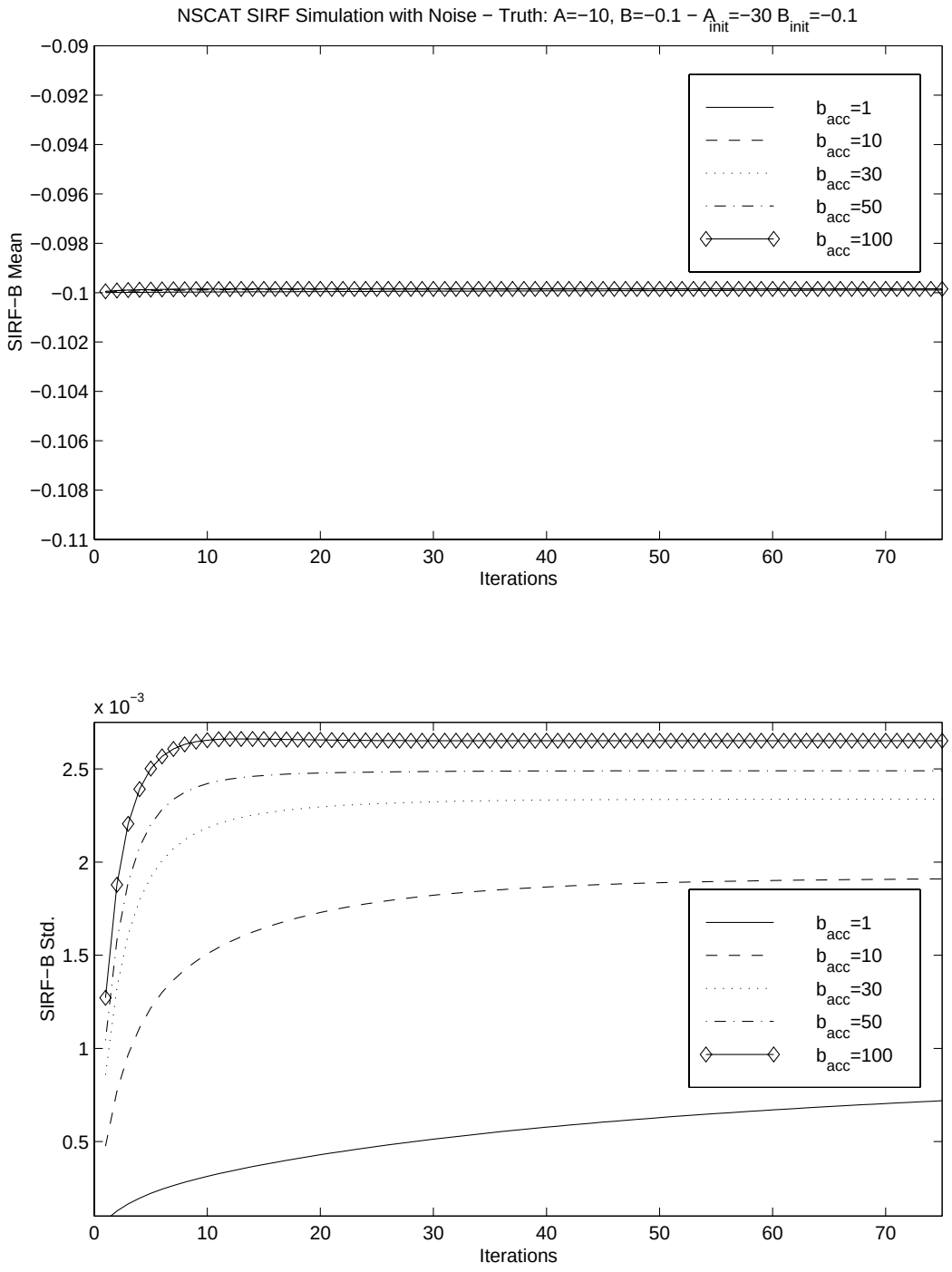

Figure 6: $\mathcal{B}$ value means and standard deviations of the SIRF simulation images with constant truth images $\mathcal{A}$=-10.0 and $\mathcal{B}$=-0.1. Initialization values are $\mathcal{A}_{init}$=-30.0 and $\mathcal{B}_{init}$=-0.1. Different values of $\mathcal{B}$ update weight are used.

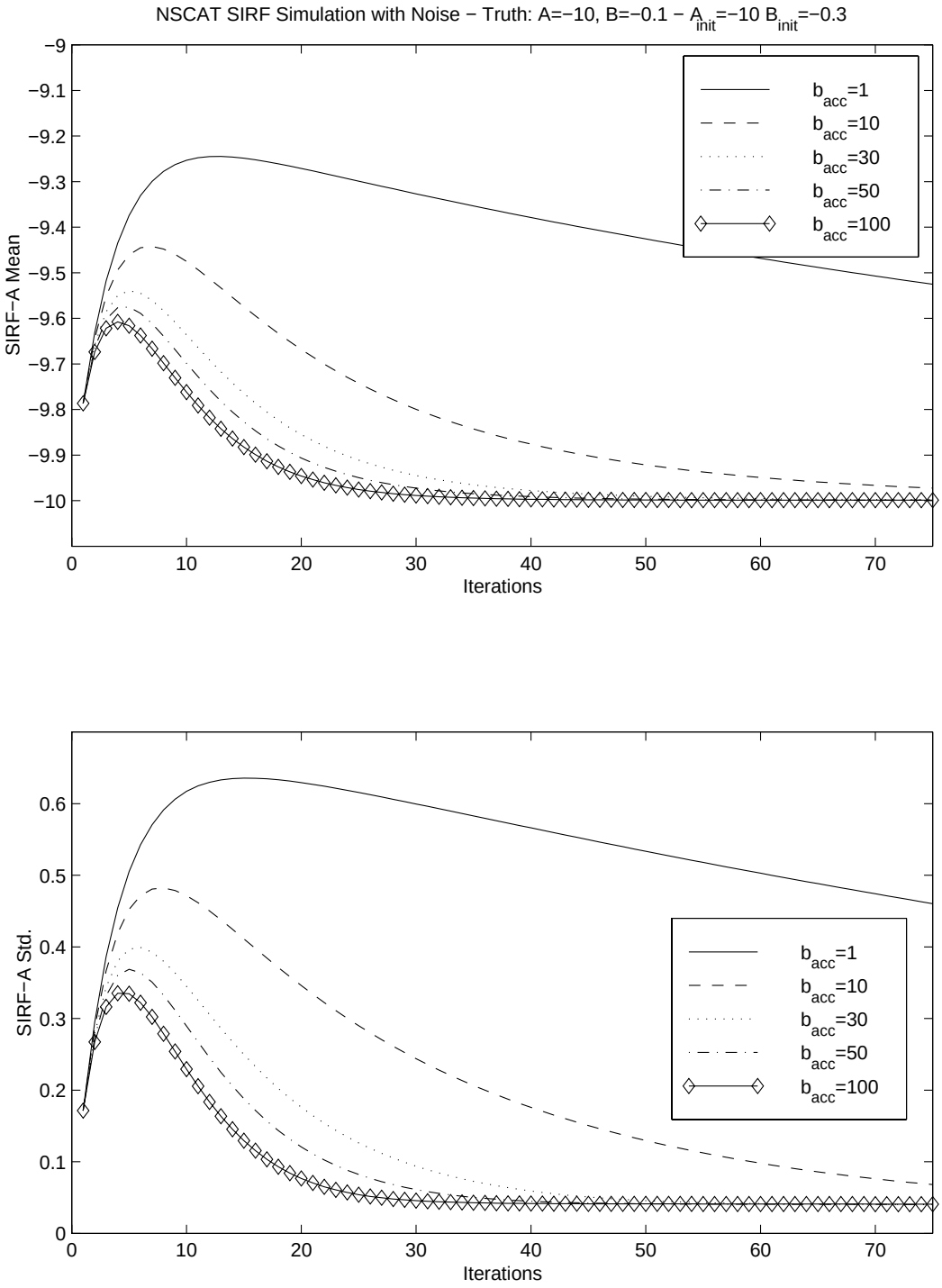

Figure 7: $\mathcal{A}$ value means and standard deviations of the SIRF simulation images with constant truth images $\mathcal{A}$=-10.0 and $\mathcal{B}$=-0.1. Initialization values are $\mathcal{A}_{init}$=-10.0 and $\mathcal{B}_{init}$=-0.3. Different values of $\mathcal{B}$ update weight are used.

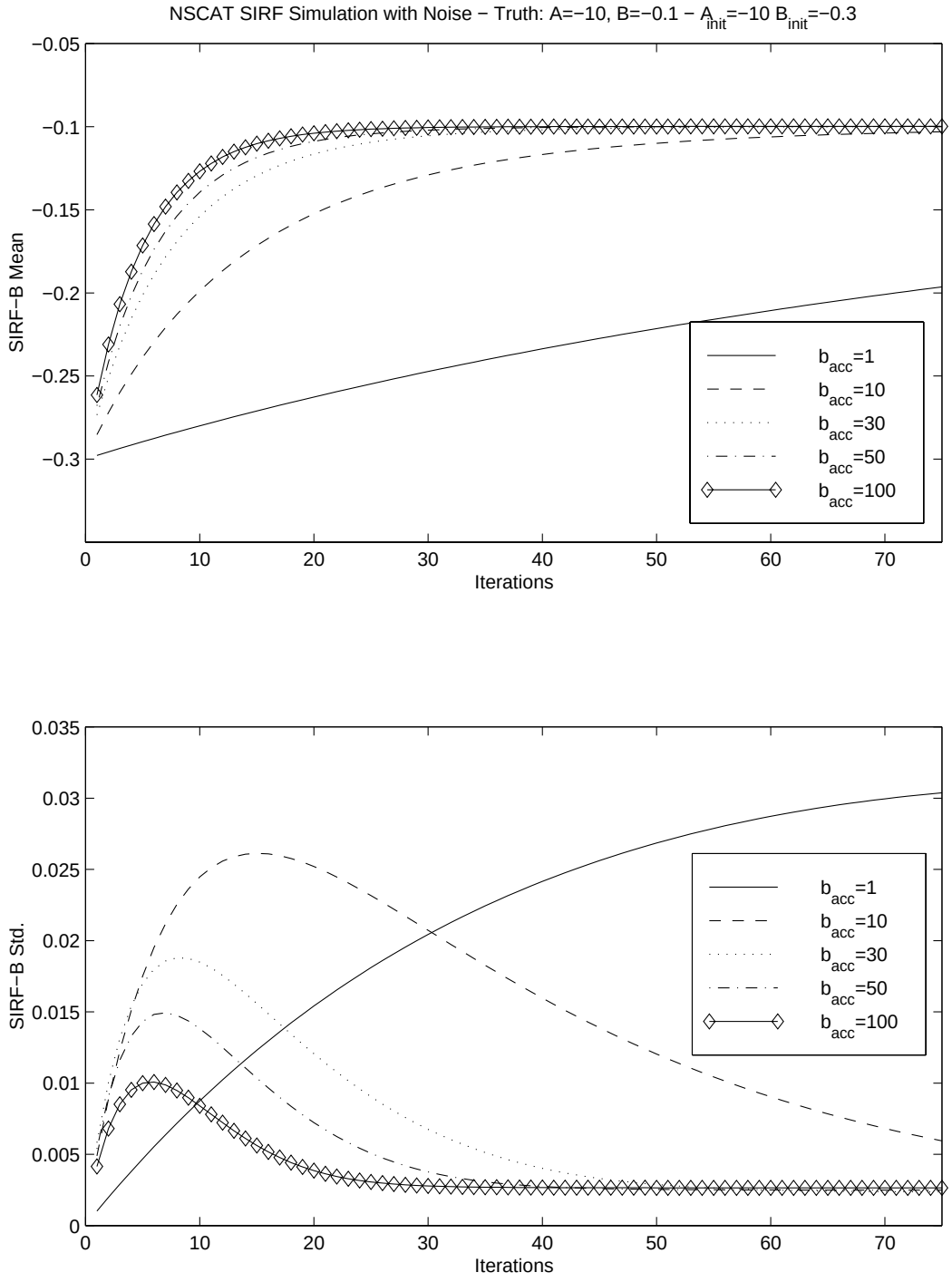

Figure 8: $\mathcal{B}$ value means and standard deviations of the SIRF simulation images with constant truth images $\mathcal{A}$=-10.0 and $\mathcal{B}$=-0.1. Initialization values are $\mathcal{A}_{init}$=-10.0 and $\mathcal{B}_{init}$=-0.3. Different values of $\mathcal{B}$ update weight are used.

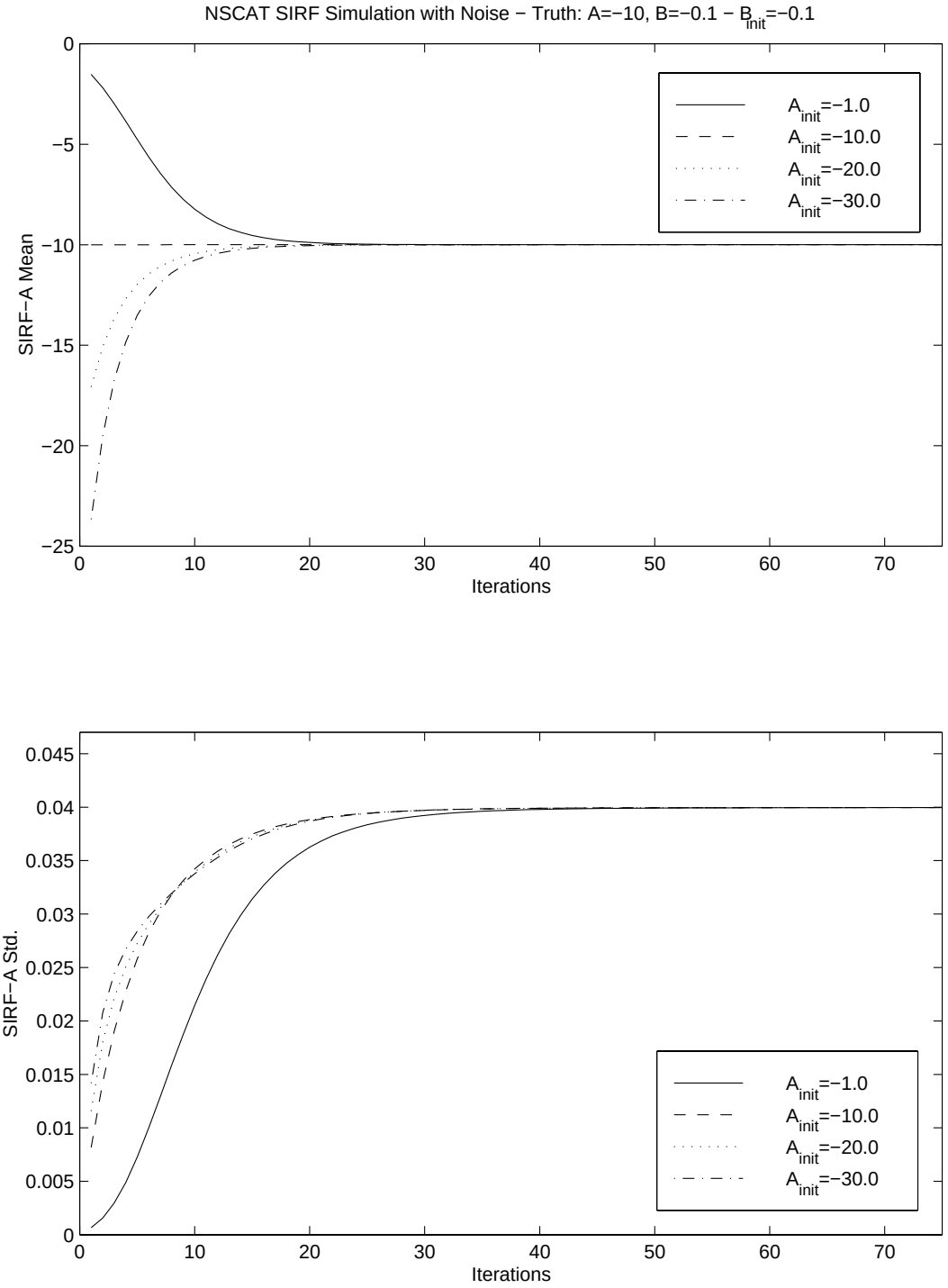

Figure 9: $\mathcal{A}$ value means and standard deviations of SIRF initialization simulation images with constant truth images $\mathcal{A}$=-10.0 and $\mathcal{B}$=-0.1. Different $\mathcal{A}_{init}$'s are used and $\mathcal{B}_{init}$ is held at the true $\mathcal{B}$ value. b_{acc}=30 for all plots.

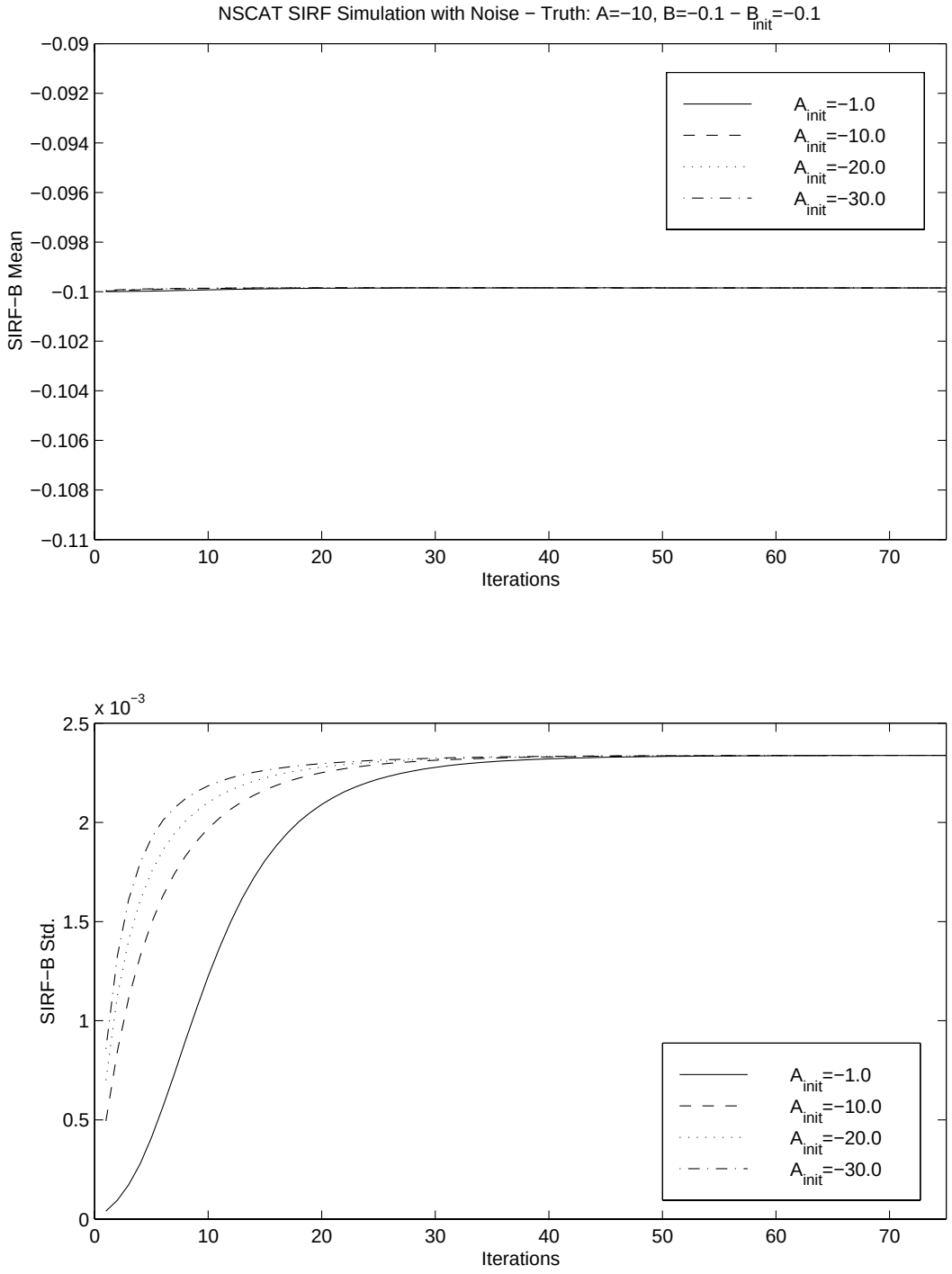

Figure 10: $\mathcal{B}$ value means and standard deviations of SIRF initialization simulation images with constant truth images $\mathcal{A}$=-10.0 and $\mathcal{B}$=-0.1. Different $\mathcal{A}_{init}$'s are used and $\mathcal{B}_{init}$ is held at the true $\mathcal{B}$ value. b_{acc}=30 for all plots.

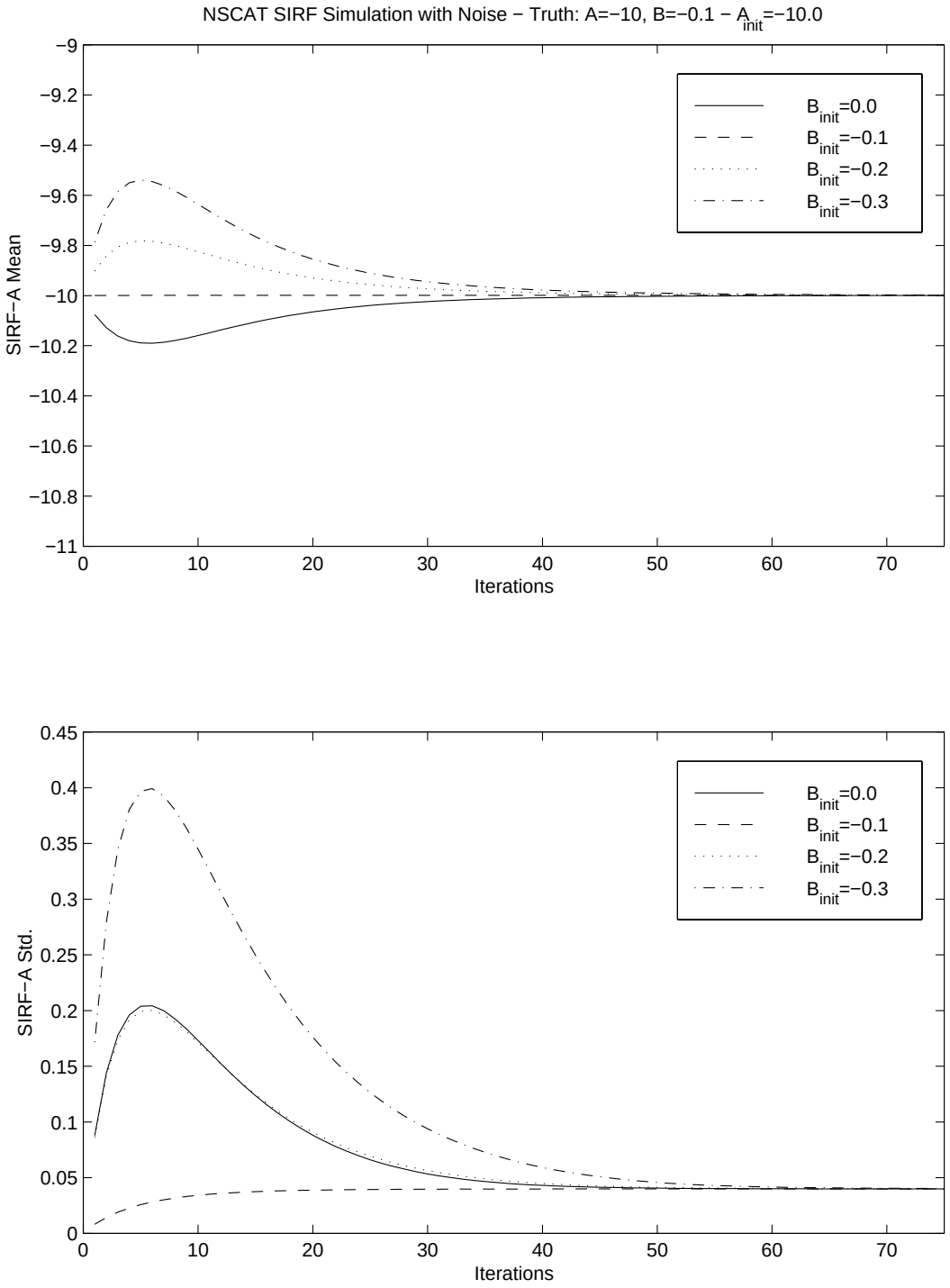

Figure 11: $\mathcal{A}$ value means and standard deviations of SIRF initialization simulation images with constant truth images $\mathcal{A}$=-10.0 and $\mathcal{B}$=-0.1. Different $\mathcal{B}_{init}$'s are used and $\mathcal{A}_{init}$ is held at the true $\mathcal{A}$ value. b_{acc}=30 for all plots.

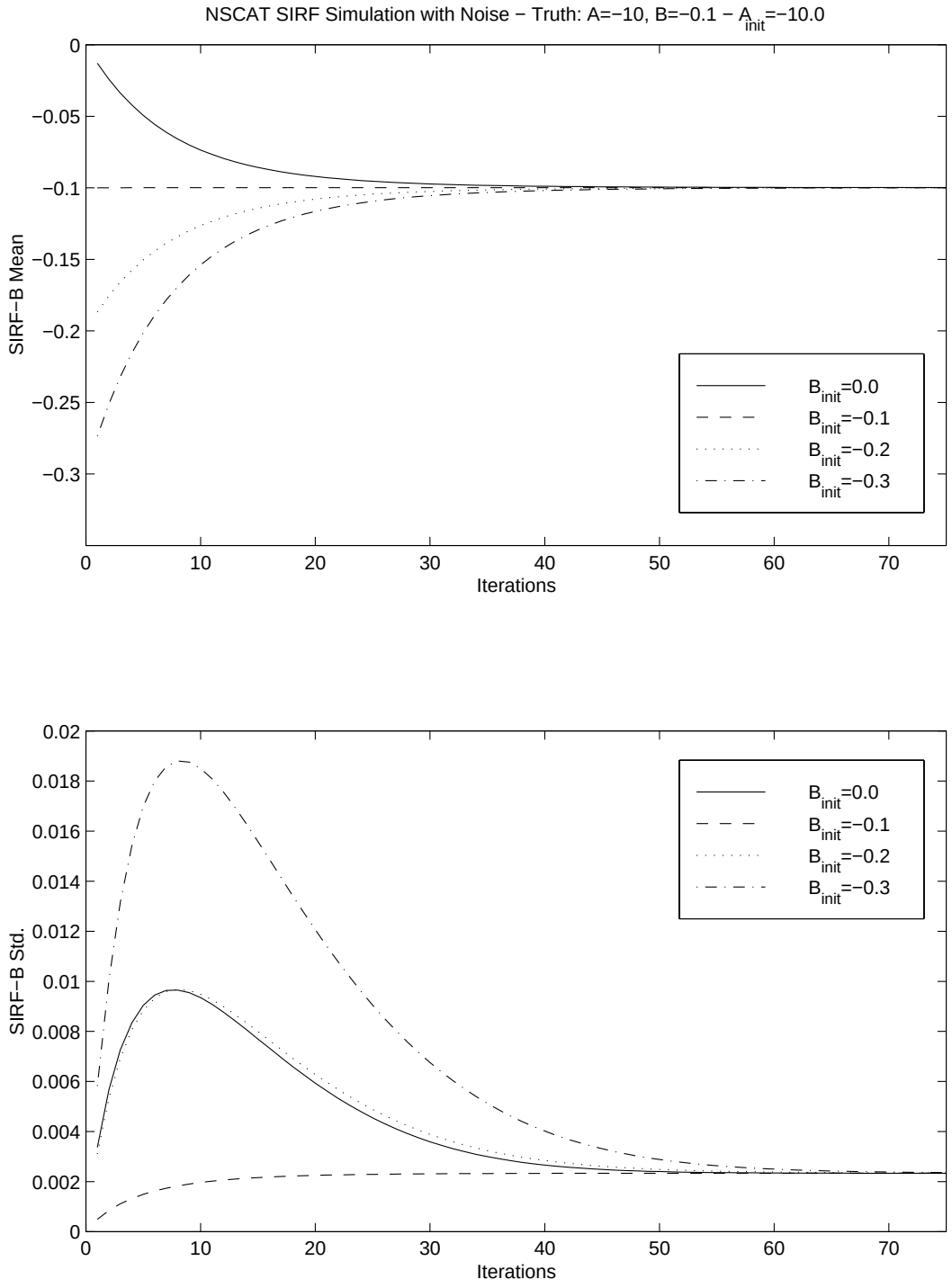

Figure 12: $\mathcal{B}$ value means and standard deviations of SIRF initialization simulation images with constant truth images $\mathcal{A}$=-10.0 and $\mathcal{B}$=-0.1. Different $\mathcal{B}_{init}$'s are used and $\mathcal{A}_{init}$ is held at the true $\mathcal{A}$ value. b_{acc}=30 for all plots.

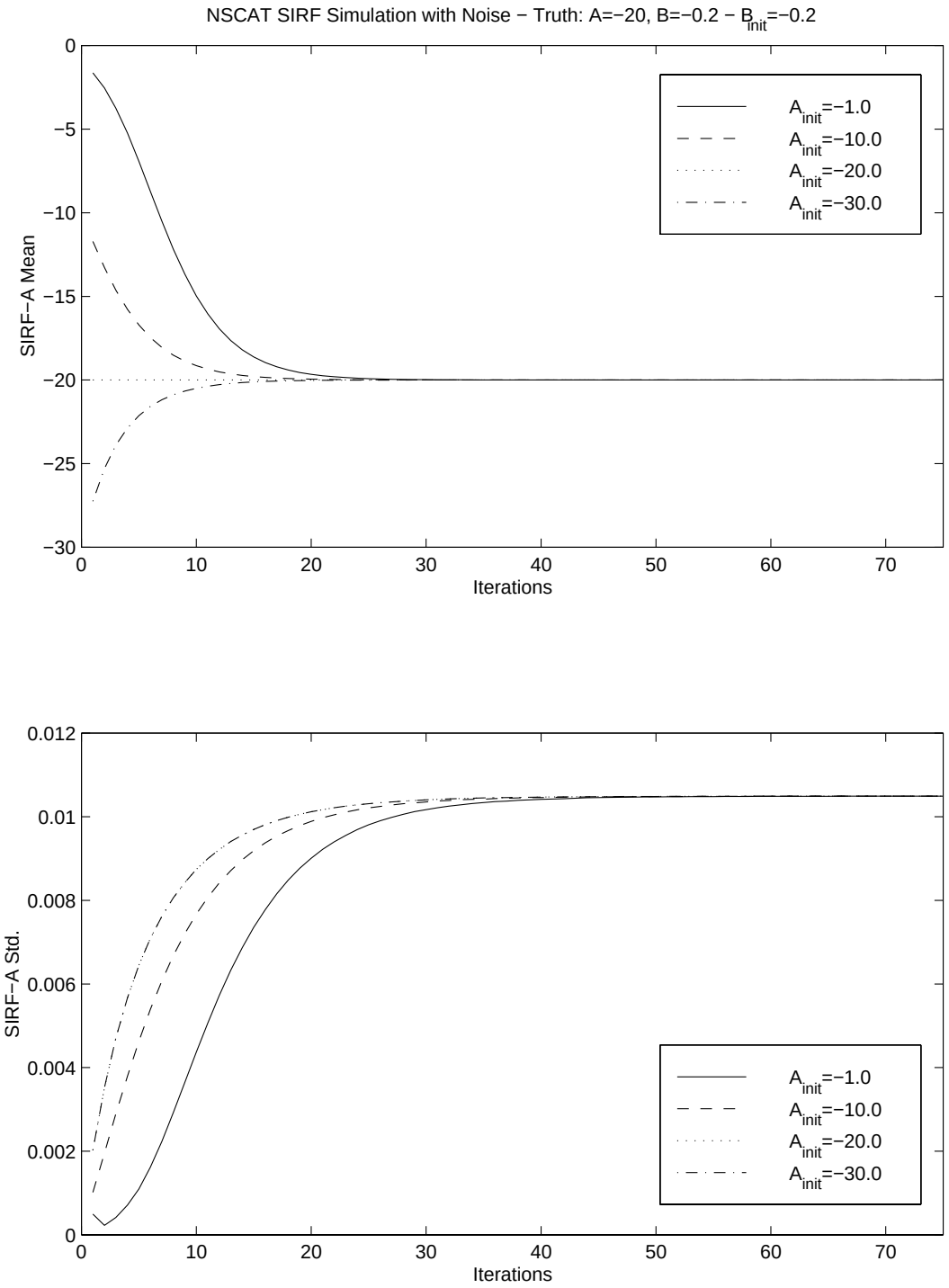

Figure 13: $\mathcal{A}$ value means and standard deviations of SIRF initialization simulation images with constant truth images $\mathcal{A}$=-20.0 and $\mathcal{B}$=-0.2. Different $\mathcal{A}_{init}$'s are used and $\mathcal{B}_{init}$ is held at the true $\mathcal{B}$ value. b_{acc}=30 for all plots.

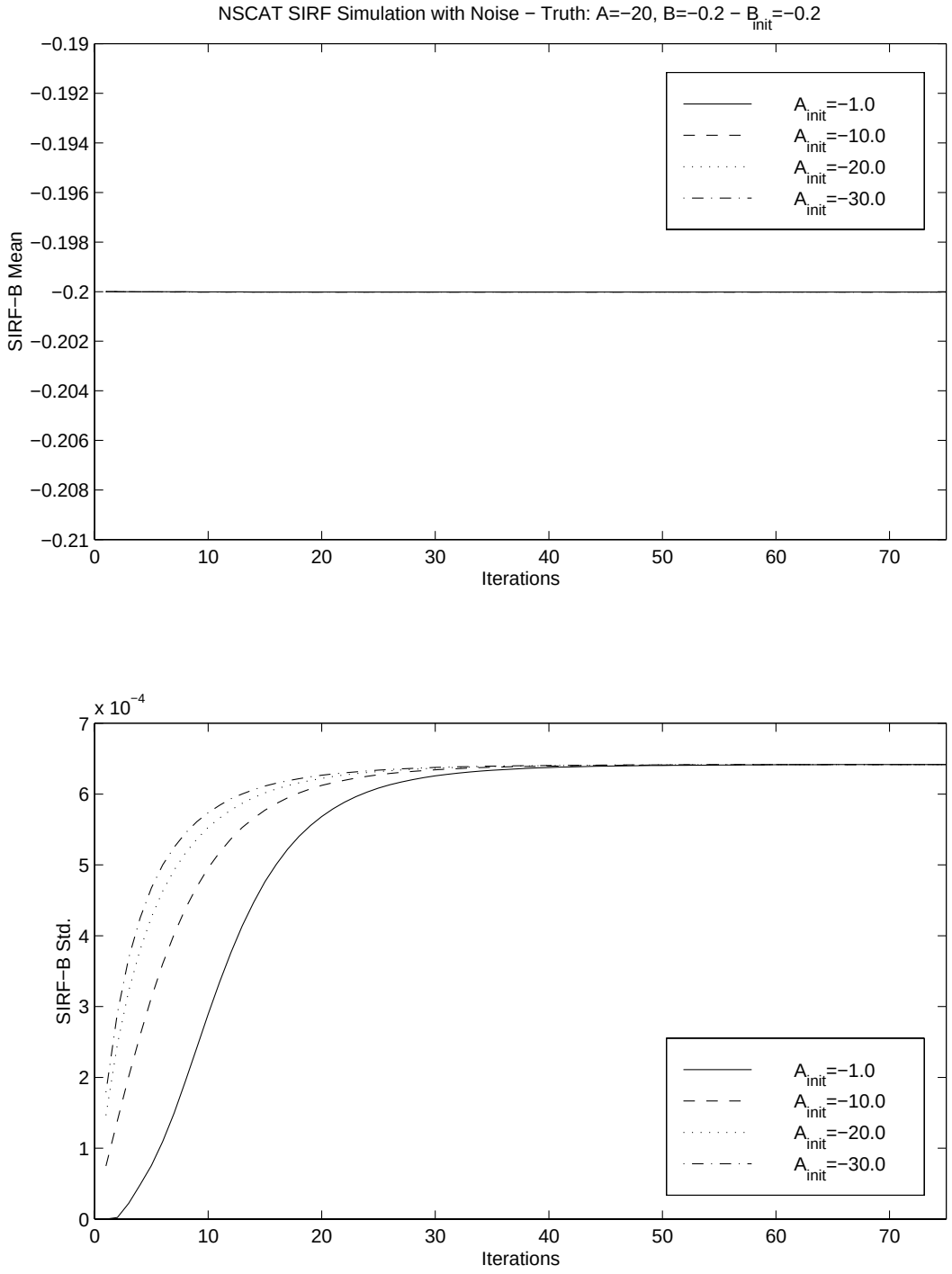

Figure 14: $\mathcal{B}$ value means and standard deviations of SIRF initialization simulation images with constant truth images $\mathcal{A}$=-20.0 and $\mathcal{B}$=-0.2. Different $\mathcal{A}_{init}$'s are used and $\mathcal{B}_{init}$ is held at the true $\mathcal{B}$ value. b_{acc}=30 for all plots.

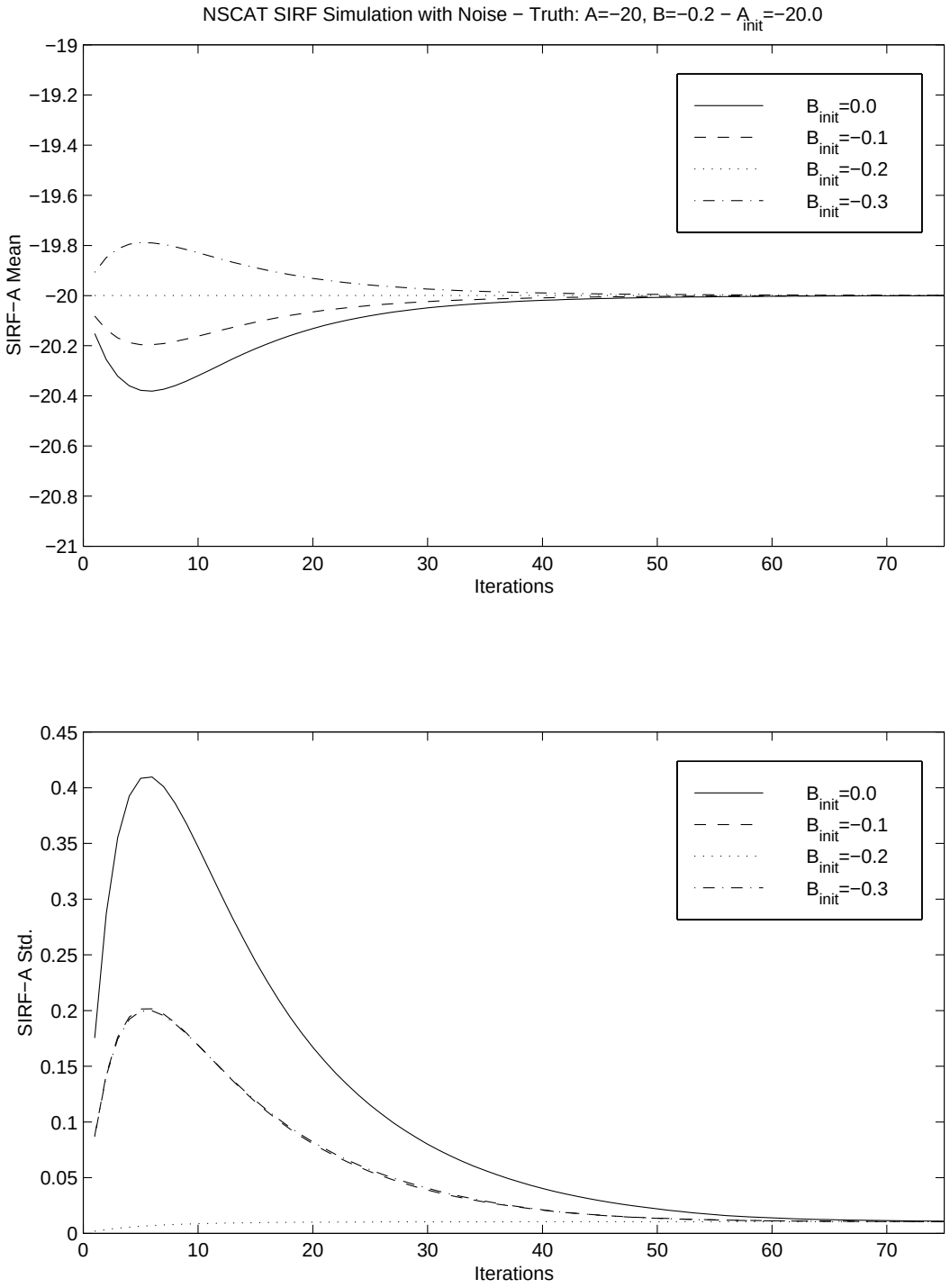

Figure 15: $\mathcal{A}$ value means and standard deviations of SIRF initialization simulation images with constant truth images $\mathcal{A}$=-20.0 and $\mathcal{B}$=-0.2. Different $\mathcal{B}_{init}$'s are used and $\mathcal{A}_{init}$ is held at the true $\mathcal{A}$ value. b_{acc}=30 for all plots.

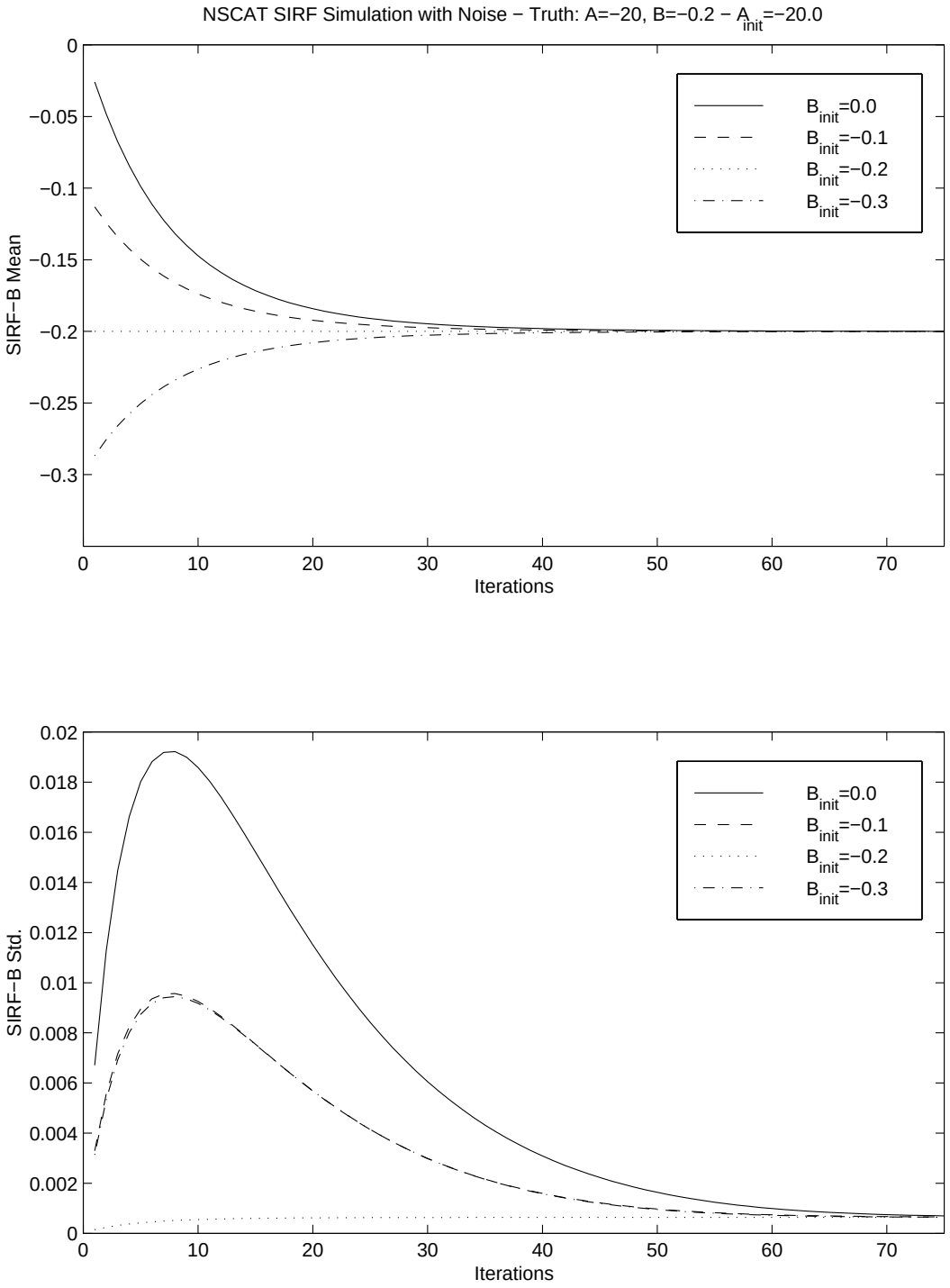

Figure 16: $\mathcal{B}$ value means and standard deviations of SIRF initialization simulation images with constant truth images $\mathcal{A}$=-20.0 and $\mathcal{B}$=-0.2. Different $\mathcal{B}_{init}$'s are used and $\mathcal{A}_{init}$ is held at the true $\mathcal{A}$ value. b_{acc}=30 for all plots.

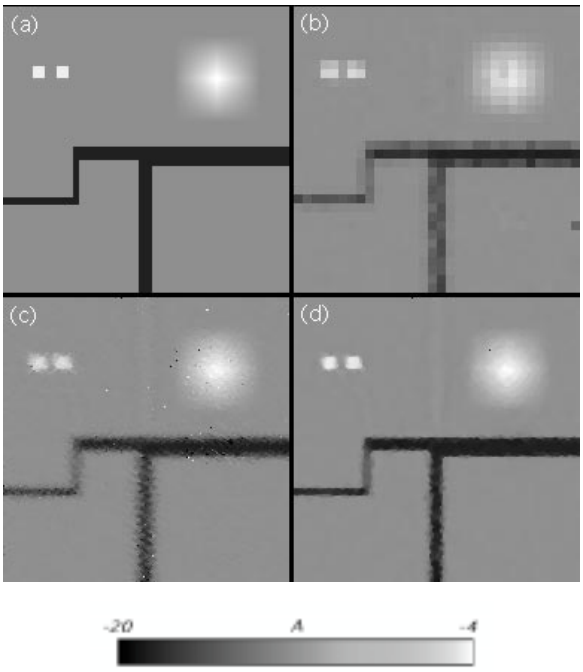

Figure 17: Reconstructed simulation $\mathcal{A}$ images with noise added. (a) Truth image, (b) Nonenhanced image, (c) AVE image, and (d) SIRF image using optimum SIRF parameters.

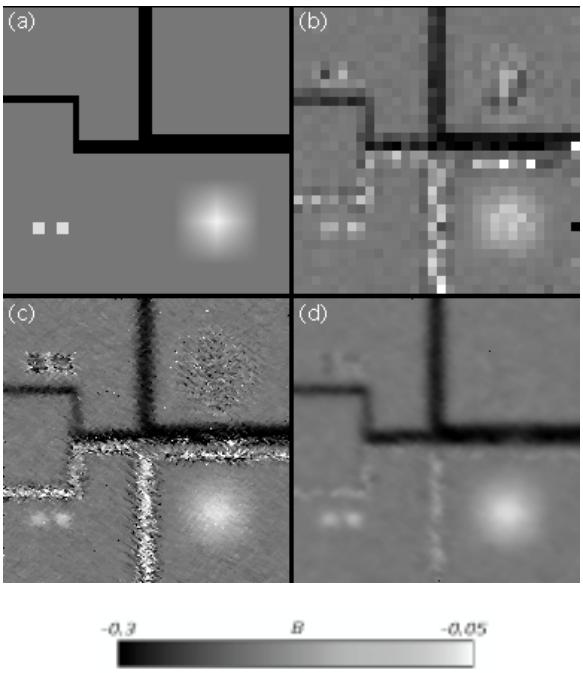

Figure 18: Reconstructed simulation $\mathcal{B}$ images with noise added. (a) Truth image, (b) nonenhanced image, (c) AVE image, and (d) SIRF image using optimum SIRF parameters.

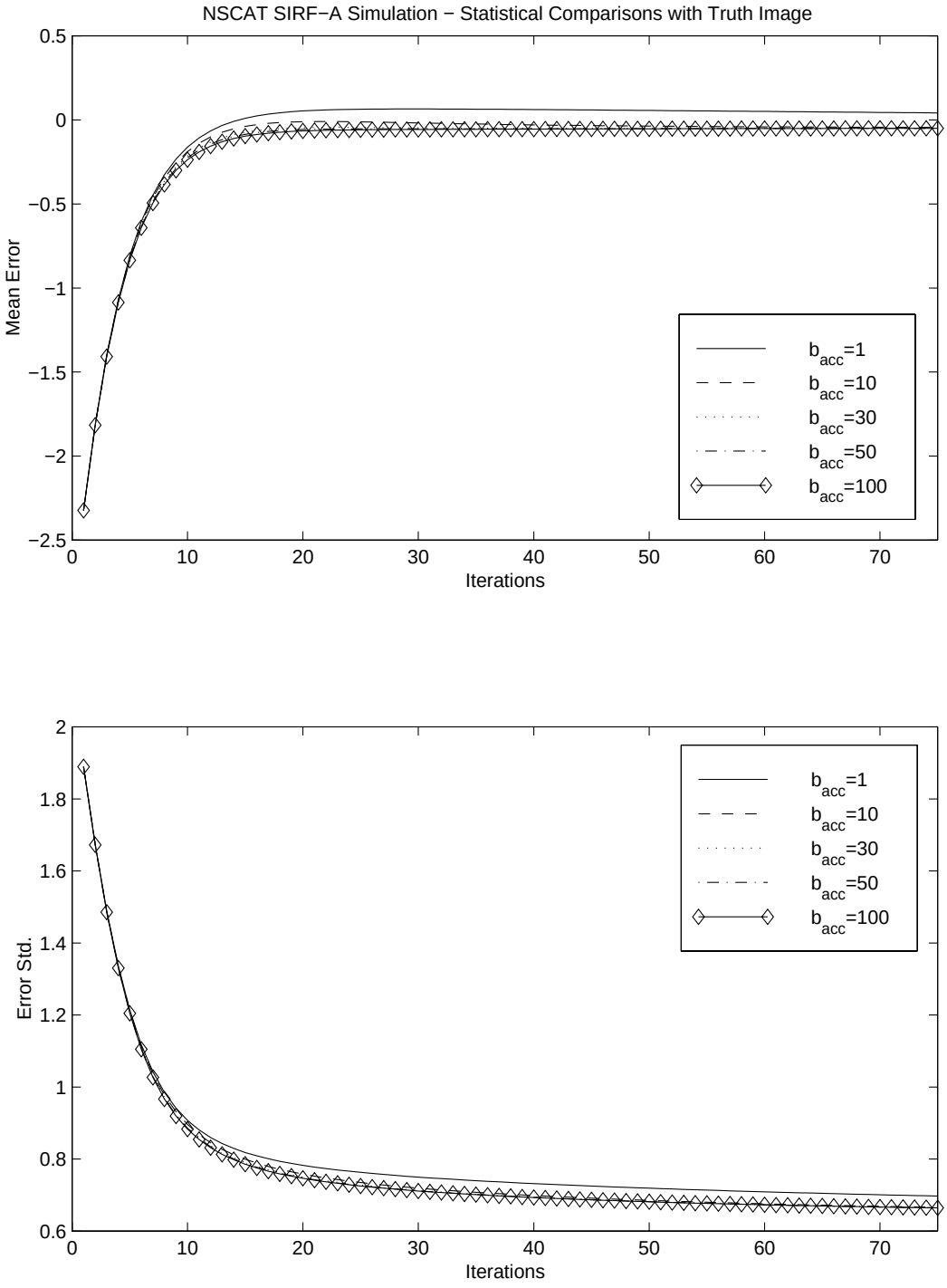

Figure 19: Mean error and error standard deviation of the SIRF $\mathcal{A}$ images for the noiseless and noisy cases.

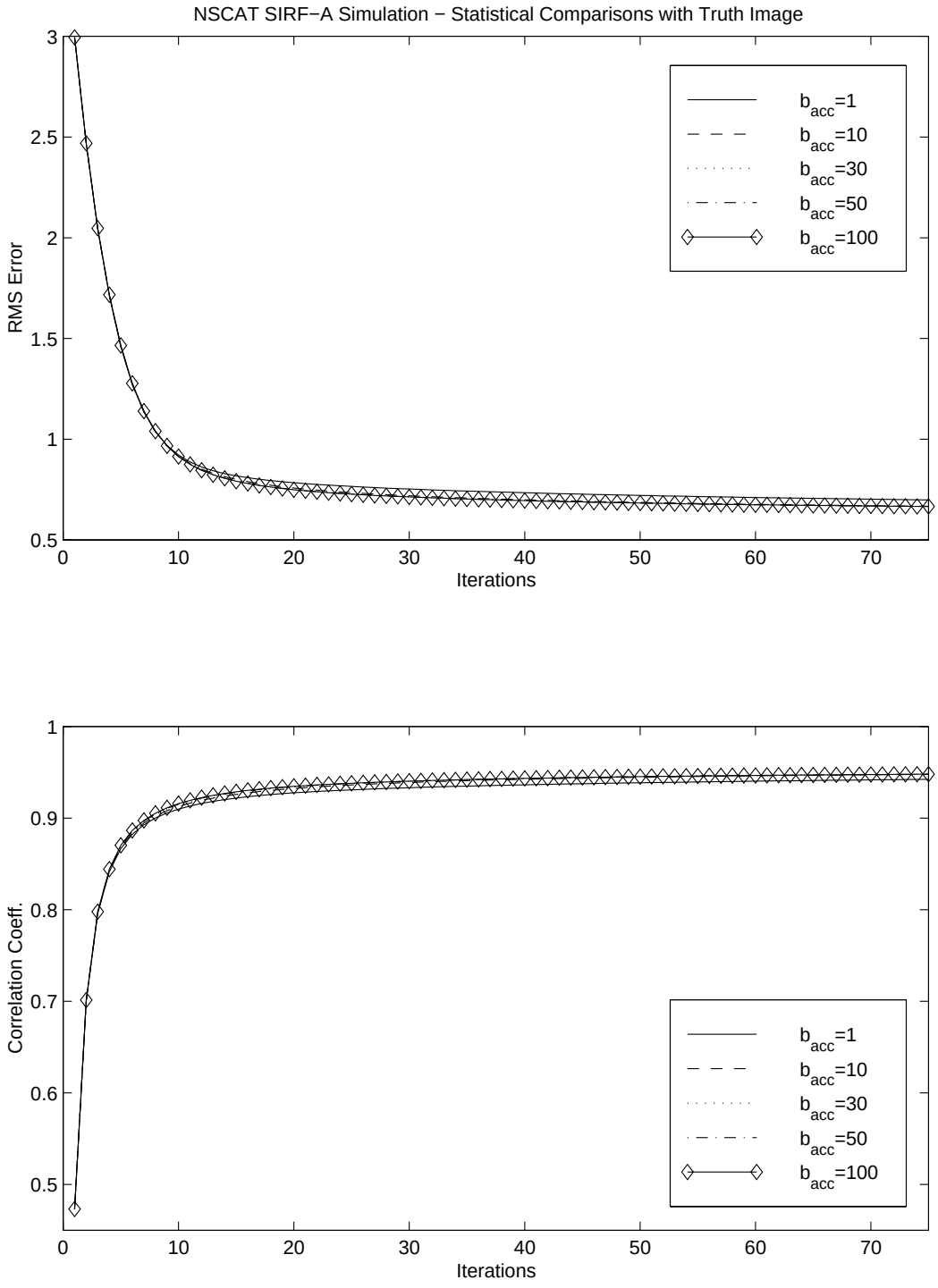

Figure 20: RMS error and correlation coefficient of the SIRF $\mathcal{A}$ images for the noiseless and noisy cases.

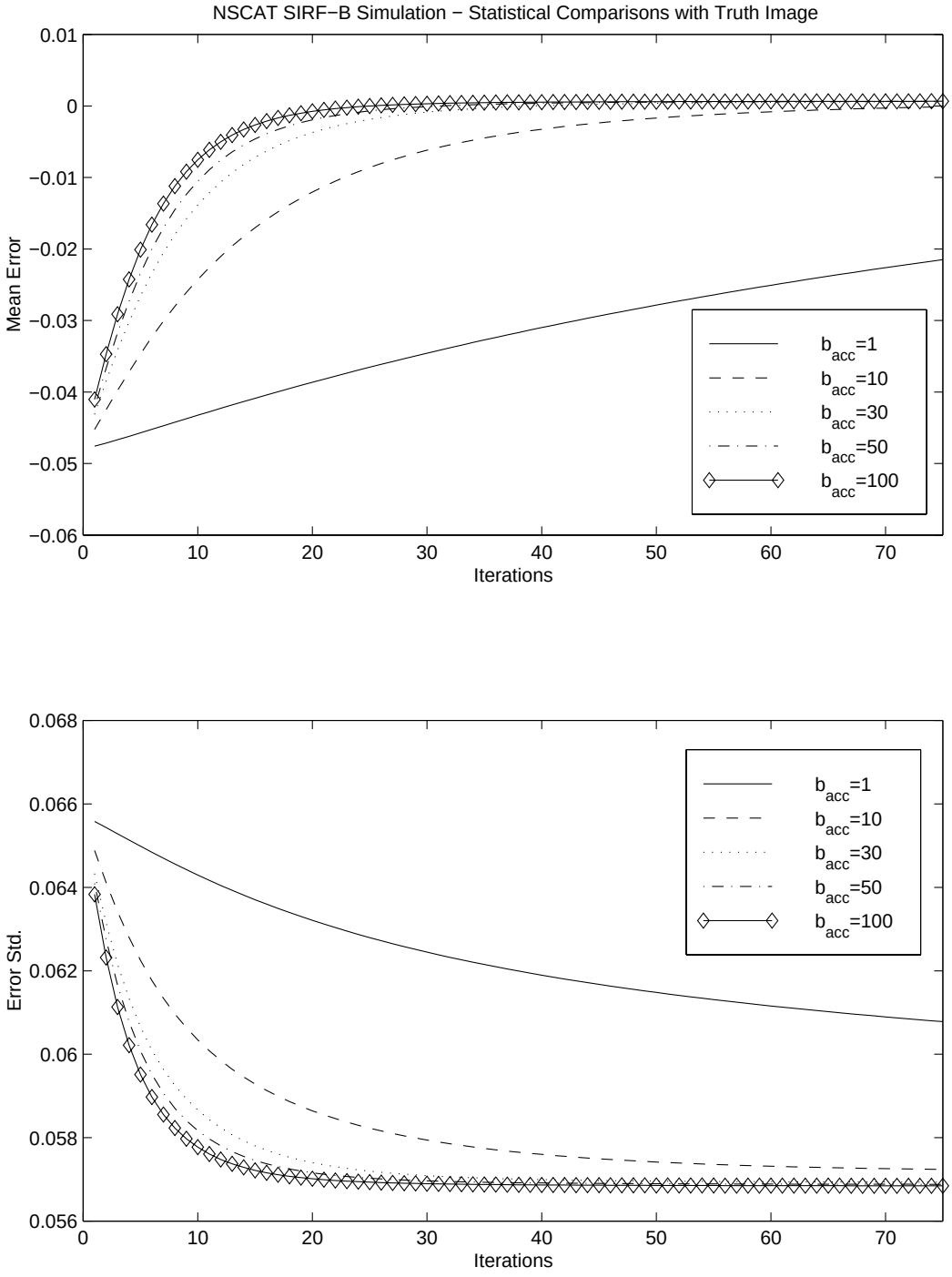

Figure 21: Mean error and error standard deviation of the SIRF $\mathcal{B}$ images for the noiseless and noisy cases.

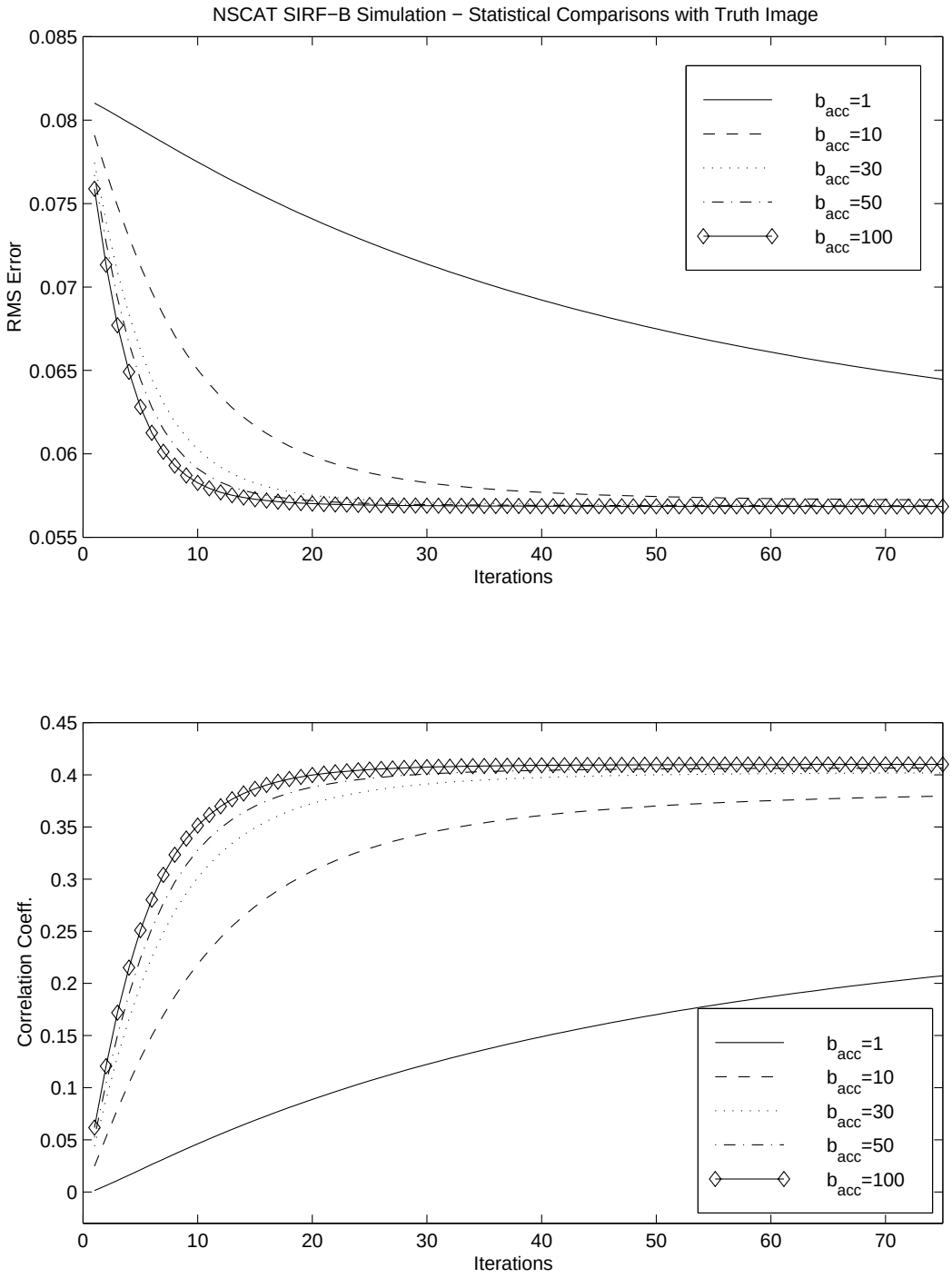

Figure 22: RMS error and correlation coefficient of the SIRF $\mathcal{B}$ images for the noiseless and noisy cases.

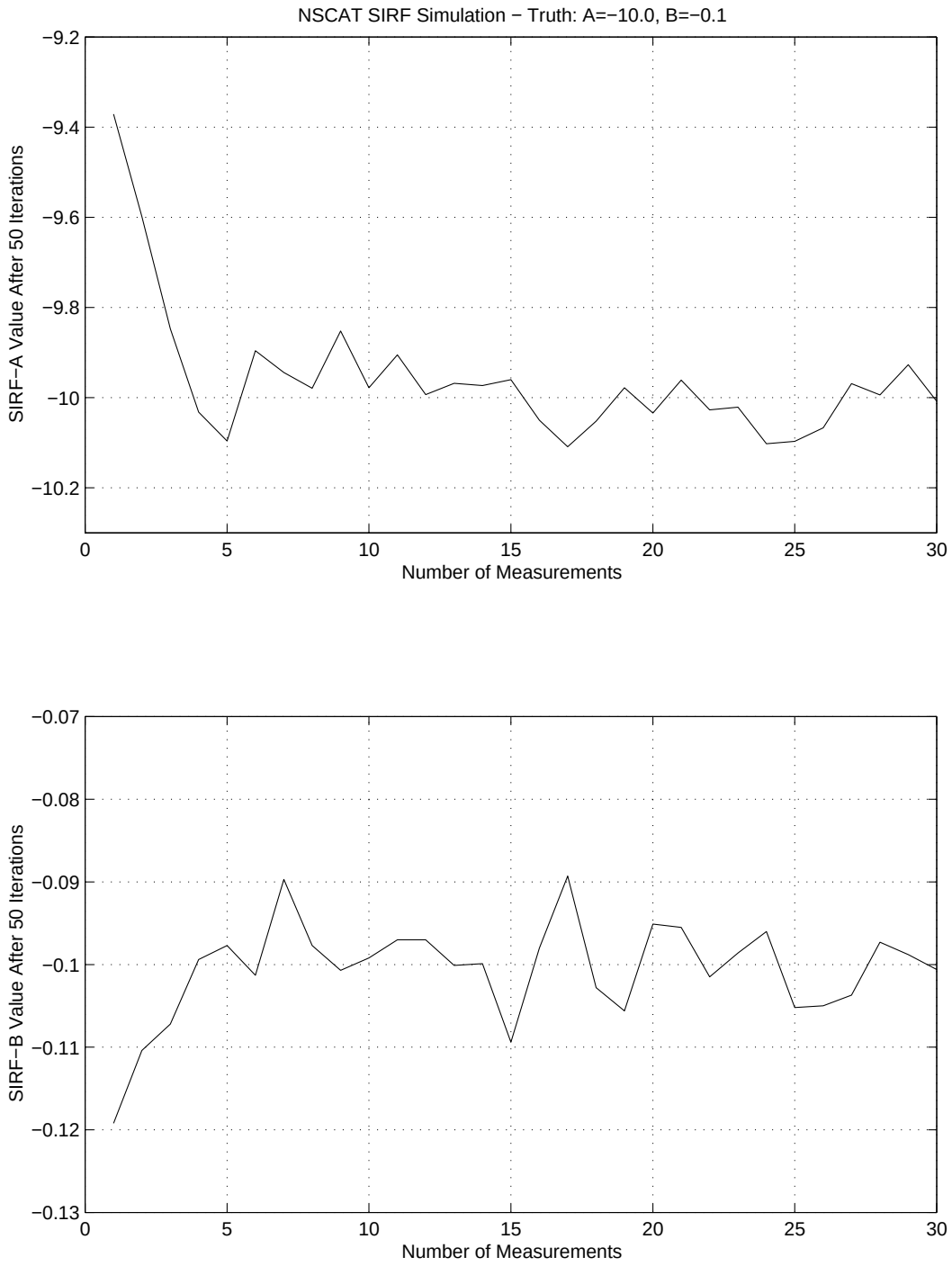

Figure 23: SIRF $\mathcal{A}$ and $\mathcal{B}$ estimates plotted vs. the number of measurements. The true values are $\mathcal{A}$=-10.0 and $\mathcal{B}$=-0.1. The estimates may be poor unless there are at least 5 samples.

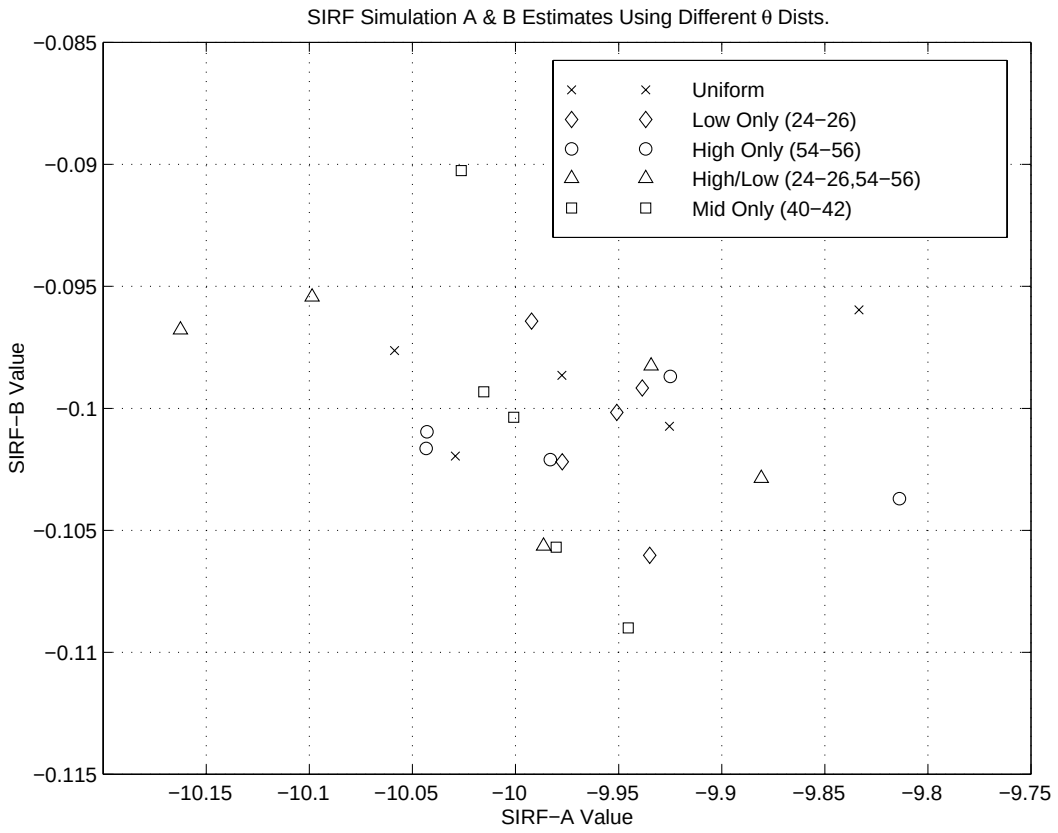

Figure 24: Plot of estimates of $\mathcal{A}$ and $\mathcal{B}$ values with different measurement incidence angle distributions. Eight measurements were used for each SIRF estimate. The true values are $\mathcal{A}$=-10.0 and $\mathcal{B}$=-0.1.